Fine structures in sheared granular flows

William Polashenski, Jr.
Lomic, Inc., 2171 Sandy Drive, Suite 130, State College, Pennsylvania 16803

Piroz Zamankhan, Simo Mäkiharju, and Parsa Zamankhan
Laboratory of Computational Fluid Dynamics, Lappeenranta University of Technology, Fin-53851, Lappeenranta, Finland
(Received 28 November 2001; revised manuscript received 6 June 2002; published 23 August 2002)

Computer simulations were used to investigate shear flows of large numbers of viscoelastic, monosized, spherical particles in unbounded and bounded systems with solid fractions ranging from 0.16 to 0.59. A modified hard-sphere model with inelastic, instantaneous particle interactions was found to replicate some results predicted by kinetic theory in an unbounded shear flow at low and moderate solids fractions. This model was found to predict features such as particle lateral diffusive motion even for systems at solid fractions as high as 0.56. However, for higher solid fractions where phenomena such as jamming could occur, a particle dynamics model accounting for particle contacts of finite duration has been developed, in which the viscoelastic behavior of the particles was represented using a nonlinear Hertzian model. The nonlinear viscoelastic model was found to give more reasonable predictions for cluster formation than previously reported linear models, especially when accounting for surface friction in the model. However, neither frictionless nor frictional particle models could predict particle ordering in unbounded flows. As such, simulations were performed for bounded systems using both the modified hard-sphere model and the nonlinear particle dynamic model. For a bounded shear flow, particle ordering could be predicted by the hard-sphere model even in the absence of both particle friction and gravity, with the local solid fraction and wall separation distance governing the flow stability. For these conditions chain formation was found to be quite likely in the disordered layers for frictional particles. The interesting stick-slip dynamics could be clearly observed in the normal stress signal at the bottom wall. Interpretations were proposed for the complex processes observed, which could lay the foundation for further investigations in sheared dense granular systems.

DOI: 10.1103/PhysRevE.66.021303 PACS number(s): 45.70.Mg, 02.70.Ns, 64.70.Dv

I. INTRODUCTION

The progression of a nonequilibrium, dense, disordered, granular assembly toward its steady state under shearing motion appears to be highly complicated. Recently, Cates, Wittmer, Bouchaud, and Claudin [1] suggested that in a constant-volume shearing flow of a dense granular material in a Couette geometry, jamming could occur indicating a transition to the glass state which has an amorphous configuration. The dilatancy, which is the tendency of dense granular media to expand upon shearing [2], could be viewed as the constant-load counterpart of jamming. Jamming appears to occur due to the formation of anisotropic, nonstraight force chains [3,4], which are linear strings of nearly rigid particles in contact that can support the shear stress along the compressional direction indefinitely [1].

In contrast to the metastable character of the jamming process mentioned above, evidence has been reported [5] which indicates that the initially disordered configuration of shaken granular monolayers may exhibit a stable crystalline order. Moreover, experimental data [6], such as that shown in Fig. 1, suggest that an ordered phase may also be observed in rapid shear flows of smooth granular materials in a two-dimensional planar Couette geometry. Thus, in addition to their importance discussed in [7], dense granular flows may serve as experimental models for investigating general features of the transition to an ordered state from a disordered configuration. This emphasizes the importance of being able to predict whether ordering or jamming would occur in a sheared disordered granular assembly. It is worth mentioning that the surface properties had a strong effect on the experimental results of Elliot, Ahmadi, and Kvasnak [6], since they did not observe an ordered phase for shearing flow of rough granular materials. This observation highlights the importance of the nature of the interactions between grains in granular systems.

In a sheared, dry, granular system, gradients in the mean flow induce interparticle collisions, which generate fluctuations in the local mean motion of the grains. The collisions involve a nearly elastic deformation of grains whose velocities change due to forces resulting from the deformation. The collision time, which is of the order of 10^{-4} s or less, consists of a compression time during which deformation occurs and a restitution time during which the shape is restored. Since kinetic energy is degraded into heat due to the inelastic nature of deformations, external energy should continuously be provided to granular systems to prevent the system from collapsing into the solid state, which is characterized by

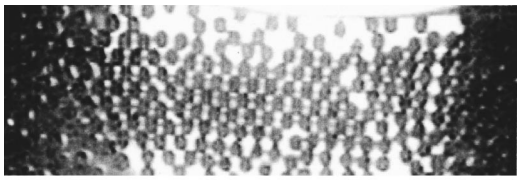

FIG. 1. Snapshot of smooth steel balls from an experiment conducted in a two-dimensional Couette geometry. Note the presence of ordering.

strong fluctuations of the forces on individual grains.

In the presence of contact friction between the grains, which induces fluctuations in the local mean rotational motion of the grains, an additional dissipation of kinetic energy into heat would be expected. Three types of friction forces may be distinguished, which are due to rolling, sliding, and adhesion (sticking) of grains. Sliding friction forces and adhesive forces could accelerate or decelerate the rotational motion of the grains, while rolling friction forces always decelerates the rotational motion. However, the physical relevance of the frictional contact between the particles remains a topic of controversy due to experimental evidence [8] that suggests that the dynamics of grains may be dominated by collisions rather than sliding contacts even in slow dense flows.

Computer simulations may play a valuable role in describing the macroscopic flow behavior resulting from the aforementioned phenomena. Attempts have been made to simulate dense granular shear flows by modeling the grains as inelastic rough spheres. One well-known method for simulating granular particles is the particle dynamic method [2,9–10]. This method assumes that the grains behave as viscoelastic particles that interpenetrate during a collision, resulting in the generation of restoring forces that can be expressed by Young's moduli of the order of 10^7 kN/m^2. The short-range interaction of particles, therefore, may result in a large gradient of the interaction force, which implies that the interaction force between the grains in contact should be calculated about 1000 times during a collision to provide accurate results. Presently a three-dimensional simulation with a large number of particles would require significant computational intensity. As such, a question arises as to whether a less computationally intensive model could predict the basic features of sheared granular flows.

Another method for the simulation of granular assemblies is the modified hard-sphere model of Alder and Wainwright [11], which has been frequently used [12,13]. In this approach, collisions are assumed to be instantaneous and the dissipation is introduced through a coefficient of restitution e and a surface friction coefficient μ and time advances from one collision to the next, rather than with an imposed time step as used in the particle dynamic methods. Although the hard-sphere model appears to be highly idealized, it can reproduce the major features observed in the experiments [13].

In the present study, the hard-sphere model will be further tested against the particle dynamic model to find out how closely the model can reproduce the interesting behavior such as jamming and ordering in sheared granular flows at high densities. To this end two quantities are introduced, which may be suitable for monitoring changes in the initially disordered state due to shearing motion. One indicator is the quantity Q_6 [14], which characterizes the average bond orientations in a system of particles. Q_6 is a rotationally invariant combination of the bond order parameters Q_{lm}, defined as $Q_{lm}=Y_{lm}[\theta(\mathbf{r}),\phi(\mathbf{r})]$. In order to evaluate the bond order parameter Q_6, particles residing within a shell of 1.4σ surrounding a given particle are considered as its near neighbors. Here σ is the particle diameter and $Y_{lm}[\theta(\mathbf{r}),\phi(\mathbf{r})]$ represents spherical harmonics associated with a bond whose midpoint is at $\mathbf{r}$, N_b is the number of bonds, $\theta(\mathbf{r})$ and $\phi(\mathbf{r})$ are the polar angles of the bond measured with respect to fixed external Cartesian coordinates. An averaged value of Q_{lm} over a suitable set of bonds in the sample is given as $\overline{Q}_{lm}=(1/N_b)\Sigma_{bonds}Q_{lm}(\mathbf{r})$. Therefore, the quantity Q_6 is defined as $Q_6=[(4\pi/13)\Sigma_{m=-6}^{6}|\overline{Q}_{lm}|^2]^{1/2}$.

A second indicator is the mean-square displacement of the particles, which is represented as a function of time, defined by $\langle\Delta r^2(t)\rangle=N^{-1}\Sigma_{i=1}^{N}\langle[\mathbf{r}_i(t)-\mathbf{r}_i(0)]^2\rangle$, where $\mathbf{r}_i(t)$ is the particle position, N represents the number of particles in the computational box, and the angular brackets, which denote the ensemble average, may be generated by using many time origins.

Rintoul and Torquato [14] showed that the first indicator for a disordered configuration approaches zero at the rate of $N_b^{-1/2}$ with the expected width of fluctuations of $0.196N_b^{-1/2}$. For example, the value of Q_6 for a system with cuboctahedral symmetry is about 0.6 [15], which makes this indicator useful for distinguishing the glass state, for which $Q_6 \approx 1/\sqrt{N_b}$, from an ordered system, since for both of these states the long-time value of $\langle\Delta r^2(t)\rangle$ [16] remains nearly constant [17].

In his experimental study of mixing in granular flows, Bridgwater [18] suggested that the motion of spherical grains in a simple shear cell is much like a random walk without a preferred direction of movement. This observation supports the use of the Einstein relationship [19] for the estimation of the diffusive motion, in an average sense, in these systems.

Note that in the wall region large variations in velocity may occur over distances of the order of a few particle diameters, which leads to particle migration in the direction normal to the plane of shear, where the particles move to regions of lower stress. As a result of this motion, which is more pronounced in moderately dense granular shearing flows, nonuniform spatial distributions of particle concentration and granular temperature develop in the direction normal to the mean flow, which results in ordinary diffusion along the concentration gradients. In the presence of a strong lateral granular temperature gradient, an extra diffusive flux of particles may be observed. Under conditions where this flux becomes significant, the application of simplified models could lead to different interpretations of measurement results in roughly similar apparatus.

For example, in systems where gravity does not affect the lateral particle diffusive motion, at nearly the same solid fractions, a difference of four orders of magnitude exists [20] between the values of the dimensionless transverse diffusion coefficient, defined as $D^*=D/\sigma^2\dot{\varepsilon}$, measured by Menon and Durian [8], and the values calculated from the results of Natarajan, Hunt, and Taylor [21]. Here, σ represents the diameter of the particles, $\dot{\varepsilon}$ is the shear rate, and D is the self-diffusion coefficient. It is unclear whether this difference is due to the inaccuracy of one (or both) of the experimental procedures (such as solid fraction measurements), or to some other reason, such as misinterpretation of the results using simplified theories.

Analyzing the observations of Menon and Durian, Denniston and Li [22] pointed out that the value of $\langle\Delta r^2(t)\rangle$ at

long times could be considered as being almost constant, indicating that diffusion was very limited. This could be due to the particles being trapped in the almost permanent cages formed by their neighbors. However, at long times the indicator $\langle \Delta r^2(t) \rangle$ for a granular assembly in the gravity driven flow of Natarajan, Hunt, and Taylor [21] increases linearly with time. This observation suggests a fluidlike behavior in a monodisperse granular flow at high average solid fractions. Surprisingly, they suggested that the average solid fraction in the system was in the range of $0.55 < \Phi_s < 0.7$, though a system with the solids' fraction $\Phi_s > 0.6$ can hardly be considered as a fluid. In this light, simulations of dense shear flows of granular material may be of value to interpret their experimental observations and could even suggest a more reasonable value for solids fraction in [21] based on the measured values of D^*.

Much of the present knowledge about particle diffusivity in shearing flows of a granular assembly has been derived from simulations. These include the calculation of the self-diffusion coefficient in a bounded system by Savage and Dai [23] and computer simulations of the anisotropic diffusion tensor for an unbounded system by Campbell [12]. Using a kinetic theory analysis, Savage and Dai [23] derived an expression for the self-diffusion coefficient, which reduces to the classical Chapman-Enskog result [24] in the limit of perfectly elastic particles. Apparently, the theoretical self-diffusion coefficients were in excellent agreement with those obtained from the simulations at low densities. However, the applicability of the theoretical expression was questioned at higher densities, since the numerical result for self-diffusion exceeded the theoretical value. This discrepancy might be attributed to an enhancement of the velocity correlations due to the excitation of slowly decaying collective motions in the flowing granular assembly. Note that Savage and Dai [23] did not consider particle diffusivity at high solid fractions, at which either ordering or a glass transition might occur. However, Campbell [12] reported the absence of particle diffusive motion at a solid fraction of 0.56, although he did not discuss whether the granular assembly had undergone crystallization, or a transition to the glass state had occurred in his system. In light of the above, a general study of the diffusion processes in granular materials appears to be lacking.

One of the aims of this paper is to set forth a preliminary framework for the analysis of shear-induced diffusion in a bounded granular material at high shear rates. To this end, a comprehensive model was developed for the diffusive processes involved in a rapid shear flow using the recently developed revised Enskog theory [25] to obtain formal expressions for the particle diffusion coefficient, particle thermal diffusion coefficient [26], and coefficient of mobility.

To obtain an increased understanding of the aforementioned mechanisms for the diffusive displacement of the particles in bounded granular materials, it would be quite useful to compare the theoretical predictions with the simulation results. Another purpose of this study, therefore, is to investigate further the issues such as ordering and jamming in the granular assembly. It has been reported that the particle roughness, which induces fluctuations in rotational motion, has a significant effect on the formation of force chains [1]. To address this issue, the simulations were divided into two main groups. In one set of simulations (rough particle simulations) the frictional contact force between the particles governs the flow dynamics, and in the other group (smooth particle simulations) the dynamics of grains is dominated by inelastic collisions.

Starting from a low solid fraction, namely, $\Phi_s \approx 0.16$, where the behavior of the system appears to be less complex, the solid fraction was increased carefully up to $\Phi_s \approx 0.58$, with the goal of examining the conditions for which the fluid would become ordered and the conditions for which jamming would occur. For low solid fractions, there are a very large number of disordered states in which spheres can arrange themselves, which causes the fluid to be thermodynamically stable. By contrast, for a dense system there are much fewer allowable disordered configurations. Therefore, at short times the instabilities could lead to the formation of a nucleation point, which at longer times results in an ordered region surrounded by low density regions. As pointed out by Johnson and Jackson [27], not all the granular material is sheared uniformly in such a system. The ordered region withstands shear, while in the low density regions, the shearing motion is enhanced, reducing the tendency of jamming of the system. Note that jamming can be viewed as a spontaneous transition to a metastable disordered configuration that withstands shear.

Although the picture described above is quite detailed, the actual behavior of sheared granular materials can be even more complex than has been indicated above. For example, in the experiments of Miller, O'Hern, and Behringer [4], the force fluctuations were measured at the wall for a dense granular flow in a Couette geometry. They observed a strongly non-Gaussian probability distribution in the time series for the normal stress, which exhibits fat tails indicative of an underlying complex dynamics with long correlation times. Interestingly, a shell model of magnetohydrodynamics turbulence produces a time series of energy dissipation as defined in [28], with the intermittent spikes of dissipation quite similar to the intermittent spikes in the data of Miller, O'Hern, and Behringer [4].

Another example is the observation of the stick-slip motion only below a critical shear rate in the shearing of cohesionless glass spheres in an annular, parallel-plate shear cell by Hanes and Inman [29]. In these systems a constant-volume shear flow may not be achieved due to the tendency of dense granular media to expand upon shearing. Analyzing the shearing flow of frictional disks confined between solid walls under a constant load, Thompson and Grest [2] pointed out that in the presence of gravity the system is unstable at shear rates less than a critical shear rate, exhibiting a stick-slip motion consistent with the experimental observations. This oscillatory motion could be due to periodic dilatancy transition and gravitational compactification. It is remarkable that a similar stick-slip dynamics has also been observed in the shearing motion of a thin microscopic fluid film confined between solid walls where the role of gravity may not be significant [30]. The similarity could indicate analogies between the statistical physics of these systems, suggesting that a more comprehensive understanding of the flow dynamics

may be obtained by comparing the results of the shearing flow of a granular material in the absence and in the presence of the gravity. Such information is invaluable in the development of advanced theories capable of describing flows at high solid fractions, which are of real significance in facilitating the design of practical granular flow systems.

The organization of the present paper is as follows. In Sec. II, a description is given of the computer simulation methods and the physical relevance of the simulations. Section III presents the simulation results for unbounded granular shear flows. Comparisons are made between the hard-sphere model and previous results from kinetic theory. For higher solid fractions, simulations using the particle dynamic model are performed, including comparisons between linear and nonlinear models of viscoelastic particle behavior. In Sec. IV, simulations of bounded shear flows are performed to investigate the formation of an ordered phase. This behavior highlights the importance of the local solid fraction and wall separation on the stability of the shear flows of a granular material. In this section the results of the wavelet analysis are also presented, which may interpret the findings in the light of phenomena observed in physical systems such as the existence of stick-slip dynamics, characterized by harmonic frequencies. Particle diffusion in low and moderately dense systems is also analyzed using a comprehensive model based on the revised Enskog theory of granular fluids and on Grad's method of moments. A part of the formulation is presented in the Appendix, along with formal expressions for the particle diffusion coefficient, particle thermal diffusion coefficient, and coefficient of mobility [31]. The computer simulations were modified to include the effects of gravity to investigate the bounded sheared systems under constant volume as well as fixed normal load. Interesting features such as the dilatancy of granular media and stick-slip dynamics are explored and as a result fresh interpretations are proposed for these complex processes. Finally, the concluding remarks are given in Sec. V.

II. MATHEMATICAL MODELS

In the present study, simulations of granular assemblies were carried out by means of the modified hard-sphere model of Alder and Wainwright [11]. Simulations were then carried out using the particle dynamic model [2,9,10], and the corresponding sets of results were compared. The model development for each approach will be described in the following sections.

A. Modified hard-sphere model

In the modified hard-sphere model [12,13], the grains are assumed to interact repulsively [32,33], and the inelasticity of the grains is taken into account through the normal coefficient of restitution, e. The restitution coefficient relates the precollision and postcollision relative velocities of the two points of impact on the particle surfaces:

$$(\mathbf{V}_{ij}'^{\,\mathrm{imp}}\cdot\hat{\mathbf{k}})\hat{\mathbf{k}}=-e(\mathbf{V}_{ij}^{\mathrm{imp}}\cdot\hat{\mathbf{k}})\hat{\mathbf{k}}, \tag{1}$$

where $\hat{\mathbf{k}}$ is the unit vector directed from the center of particle i to that of particle j at the moment of impact, and $V_{ij}'^{\,\mathrm{imp}}$ indicates the postcollisional value of the relative velocity. The normal restitution coefficient decreases from unity as the normal impact velocity, $V_n=\mathbf{V}_{ij}^{\mathrm{imp}}\cdot\hat{\mathbf{k}}$, increases from zero [34]. Assuming that no plastic deformation occurs, Schwager and Pöschel [35] used the generalized Hertz theory of elastic impact for the case of viscoelastic collisions and suggested an approximate functional form for $e(V_n)$ as $1-e\sim V_n^{1/5}$, which appears to be in agreement with the experimental data [34]. Following this idea, the following heuristic functional form was chosen for the coefficient of restitution:

$$e(V_n^*)=1-(1-e_0)(V_n^*)^{1/5}, \tag{2}$$

where the dimensionless normal impact velocity is defined as $V_n^*=V_n/V_0$. Here, the reference coefficient of restitution, e_0, and the reference velocity V_0 are adjustable parameters of the model.

Considering the particle rotational motion, the relative velocity of the two points on the particle surfaces that come together at impact, $\mathbf{V}_{ij}^{\mathrm{imp}}$, is given by Allen and Tildesley [36],

$$\mathbf{V}_{ij}^{\mathrm{imp}}=(\mathbf{V}_i-\mathbf{V}_j)-\frac{\sigma}{2}\hat{\mathbf{k}}\times(\boldsymbol{\omega}_i+\boldsymbol{\omega}_j). \tag{3}$$

In the above equation, $\mathbf{V}_i$, $\mathbf{V}_j$, $\boldsymbol{\omega}_i$, and $\boldsymbol{\omega}_j$ are the translational velocity and the spin velocity of i and j particles, respectively. For the description of the tangential forces between grains at the contact zone, Lun and Savage [37] suggested that during a collision the tangential components of $\mathbf{V}_{ij}^{\mathrm{imp}}$ are changed such that

$$\hat{\mathbf{k}}\times(\mathbf{V}_{ij}'^{\,\mathrm{imp}}\times\hat{\mathbf{k}})=-\beta\hat{\mathbf{k}}\times(\mathbf{V}_{ij}^{\mathrm{imp}}\times\hat{\mathbf{k}}), \tag{4}$$

where β is the tangential coefficient of restitution. Then the conservation laws yield the following expression for the impulse:

$$\mathbf{J}=m\,\eta_1(\hat{\mathbf{k}}\cdot\mathbf{V}_{ij}^{\mathrm{imp}})\hat{\mathbf{k}}+m\,\eta_2\hat{\mathbf{k}}\times(\mathbf{V}_{ij}^{\mathrm{imp}}\times\hat{\mathbf{k}}), \tag{5}$$

where $\eta_1=\frac{1}{2}[1+e(V_n)]$, $\eta_2=\frac{1}{2}(1+\beta)\kappa/(1+\kappa)$, $\kappa=4I/(m\sigma^2)$, and m and I are the mass and the moment of inertia of the particle, respectively. The first term on the right side of Eq. (5) represents the normal impulse which is in the direction of $\hat{\mathbf{k}}$, and the second term is the tangential impulse which is in the direction perpendicular to $\hat{\mathbf{k}}$ and lies in the plane of $\hat{\mathbf{k}}$ and $\mathbf{J}$. It is worth mentioning that the kinetic energy of the particles is not necessarily conserved in collisions due to the inelasticity and roughness of the particles.

The Coulomb [38] friction law was chosen to model the friction between two colliding grains with a surface friction coefficient μ when the normal impact velocity V_n is small, namely, $\eta_2|\hat{\mathbf{k}}\times(\mathbf{V}_{ij}^{\mathrm{imp}}\times\hat{\mathbf{k}})|\geqslant\mu\eta_1|(\hat{\mathbf{k}}\cdot\mathbf{V}_{ij}^{\mathrm{imp}})\hat{\mathbf{k}}|$. Then, an expression for the tangential coefficient of restitution, β, may be found as follows:

$$\beta = -1 + \mu(1+e)\left(1+\frac{1}{\kappa}\right)\frac{|(\hat{\mathbf{k}}\cdot\mathbf{V}_{ij}^{\mathrm{imp}})\hat{\mathbf{k}}|}{|\hat{\mathbf{k}}\times(\mathbf{V}_{ij}^{\mathrm{imp}}\times\hat{\mathbf{k}})|}. \tag{6}$$

Note that negative values of β in the above expression indicate a reduction in the component of the postcollisional relative velocity perpendicular to $\hat{\mathbf{k}}$, without any change in its direction [37].

When the normal impact velocity V_n is large, namely, $\eta_2|\hat{\mathbf{k}}\times(\mathbf{V}_{ij}^{\mathrm{imp}}\times\hat{\mathbf{k}})| < \mu\eta_1|(\hat{\mathbf{k}}\cdot\mathbf{V}_{ij}^{\mathrm{imp}})\hat{\mathbf{k}}|$, then either sticking or rolling without slipping at impact may occur. During sticking contacts, both the magnitude and direction of the relative tangential velocity may change. A phenomenological constant, denoted by β_0, has been suggested by Lun and Bent [12] to characterize the restitution of velocity in the tangential direction for the sticking contact. The suggested value for this parameter for steel pucks is $\beta_0 = 0.4$ [12]. For rolling with slipping, $\beta = 0$ [39]. In this case the average normal force results in a large tangential force which decelerates the precollisional tangential velocity, $\hat{\mathbf{k}}\times(\mathbf{V}_{ij}^{\mathrm{imp}}\times\hat{\mathbf{k}})$, without slipping.

Applying the calculated values for the coefficients of restitution, the postcollisional velocities and spins, which are required to create the trajectories of the particles in the cell, can be determined using the following equations:

$$\mathbf{V}_i - \mathbf{V}_i' = \mathbf{V}_j' - \mathbf{V}_j = (\eta_1 - \eta_2)(\hat{\mathbf{k}}\cdot\mathbf{V}_{ij}^{\mathrm{imp}})\hat{\mathbf{k}} + \eta_2\mathbf{V}_{ij}^{\mathrm{imp}},$$
$$\boldsymbol{\omega}_i' - \boldsymbol{\omega}_i = \boldsymbol{\omega}_j' - \boldsymbol{\omega}_j = -\frac{2\hat{\mathbf{k}}}{\kappa\sigma}\times[\eta_2\hat{\mathbf{k}}\times(\mathbf{V}_{ij}^{\mathrm{imp}}\times\hat{\mathbf{k}})]. \tag{7}$$

Following Allen and Tildesley [36], a generalized relation was developed for the collision time calculation of a pair of particles, i and w, of diameter σ, which are located at time t at $\mathbf{r}_i$ and $\mathbf{r}_w$ having velocities $\mathbf{v}_i$ and $\mathbf{v}_w$, which experience different accelerations $\mathbf{a}_i$ and $\mathbf{a}_w$. If these particles are to collide at time $t + t_{iw}$, namely,

$$\left|\mathbf{r}_{iw} + \mathbf{V}_{iw}t_{iw} + \frac{1}{2}\mathbf{a}_{iw}t_{iw}^2\right| = \sigma, \tag{8}$$

then t_{iw} may be obtained by finding the smallest real positive root of the following quartic equation:

$$\frac{a_{iw}^2}{4}t_{iw}^4 + c_{iw}t_{iw}^3 + (\nu_{iw}^2 + d_{iw})t_{iw}^2 + 2b_{iw}t_{iw} + r_{iw}^2 - \sigma^2 = 0. \tag{9}$$

Here, a_{iw} and ν_{iw} are the values of the relative acceleration and relative velocity vectors, respectively, between particles i and w. The parameter c_{iw} is the dot product of these two vectors, namely, $c_{iw} = \mathbf{a}_{iw}\cdot\mathbf{V}_{iw}$, and the variable r_{iw} denotes the distance between the centers of the particles. The parameter $d_{iw} = \mathbf{a}_{iw}\cdot\mathbf{r}_{iw}$ represents the dot product of relative acceleration and position vectors. The dot product of the relative velocity and relative position vectors of particles i,w, is represented by b_{iw}, i.e., $b_{iw} = \mathbf{r}_{iw}\cdot\mathbf{V}_{iw}$. The solutions of Eq. (9) can be explicitly expressed by

TABLE I. Definition of variables needed for the solution of the quartic equation.

Variable	Definition
k_1	$4[(c_{iw}/a_{iw})^2 - \frac{2}{3}(\nu_{iw}^2 + d_{iw})]/a_{iw}^2$
k_2	$2^{5/3}[(2^{2/3}k_4)/(k_5+k_6)^{1/3} + (k_5+k_6)^{1/3}]/(3a_{iw}^2)$
k_3	$16[c_{iw}(\nu_{iw}^2 + d_{iw})/a_{iw}^2 - 4(b_{iw} + c_{iw}^3/a_{iw}^4)]/a_{iw}^2$
k_4	$(\nu_{iw}^2 + d_{iw})^2 - 6c_{iw}b_{iw} + 3a_{iw}^2(r_{iw}^2 - \sigma^2)$
k_5	$2(\nu_{iw}^2 + d_{iw})^3 - 18b_{iw}c_{iw}(\nu_{iw}^2 + d_{iw}) + 27a_{iw}^2b_{iw}^2 + 9(r_{iw}^2 - \sigma^2)[3c_{iw}^2 - 2a_{iw}^2(\nu_{iw}^2 + d_{iw})]$
k_6	$\sqrt{-4k_4^3 + k_5^2}$

$$t_{iw} = \begin{cases} \left[-\dfrac{c_{iw}}{a_{iw}^2} + \frac{1}{2}(k_1+k_2)^{1/2}\right] \\ \quad \pm\frac{1}{2}\left(2k_1 - k_2 + \dfrac{k_3(k_1+k_2)^{-1/2}}{4}\right)^{-1/2} \\ \left[-\dfrac{c_{iw}}{a_{iw}^2} - \frac{1}{2}(k_1+k_2)^{1/2}\right] \\ \quad \pm\frac{1}{2}\left(2k_1 - k_2 - \dfrac{k_3(k_1+k_2)^{-1/2}}{4}\right)^{-1/2}. \end{cases} \tag{10}$$

The expressions for the variables k_1, k_2, and k_3 are listed in Table I.

Neither, one, or both pairs of roots may be real. The smallest real positive root of the quartic equation (9) corresponds to particle impact. Obviously, the absence of any real positive root implies that the pair of particles will not imminently collide. In the case that the particles experience the same acceleration (e.g., gravitational acceleration), quartic equation (9) reduces to the quadratic equation given in [36].

In this approach, in which the system evolves on a collision-by-collision basis [36], the collision dynamics model is implemented for the colliding pair and then a search is initiated for the next collision. Applying this method, three-dimensional simulations of a large number of particles can be conducted in reasonably short run times.

B. Particle dynamics models

In the particle dynamics model, two stages occur during an impact. During the first stage, which is called quasielastic initial compression, the particles undergo deformation until their relative velocity vanishes. Recent experiments by Gugan [40] demonstrated that in this period, the kinetic energy of the relative motion of the particles may be stored throughout the strain field. Therefore, the elastic potential energy function used by Hertz [41] may be valid for the initial compression, suggesting that a normal repulsive contact force on particle i due to particle j is produced, whose magnitude is given by

$$|\mathbf{F}_{n,ij}| = K_n\delta_{ij}^{3/2}. \tag{11}$$

In the above equation, K_n is a constant defined as $\sigma^{1/2}/(3\chi)$ for a sphere on sphere and $\sqrt{2}\sigma^{1/2}/(3\chi)$ for a sphere on plane, $\chi = (1-\nu^2)/E$, ν is the Poisson's ratio, and E is

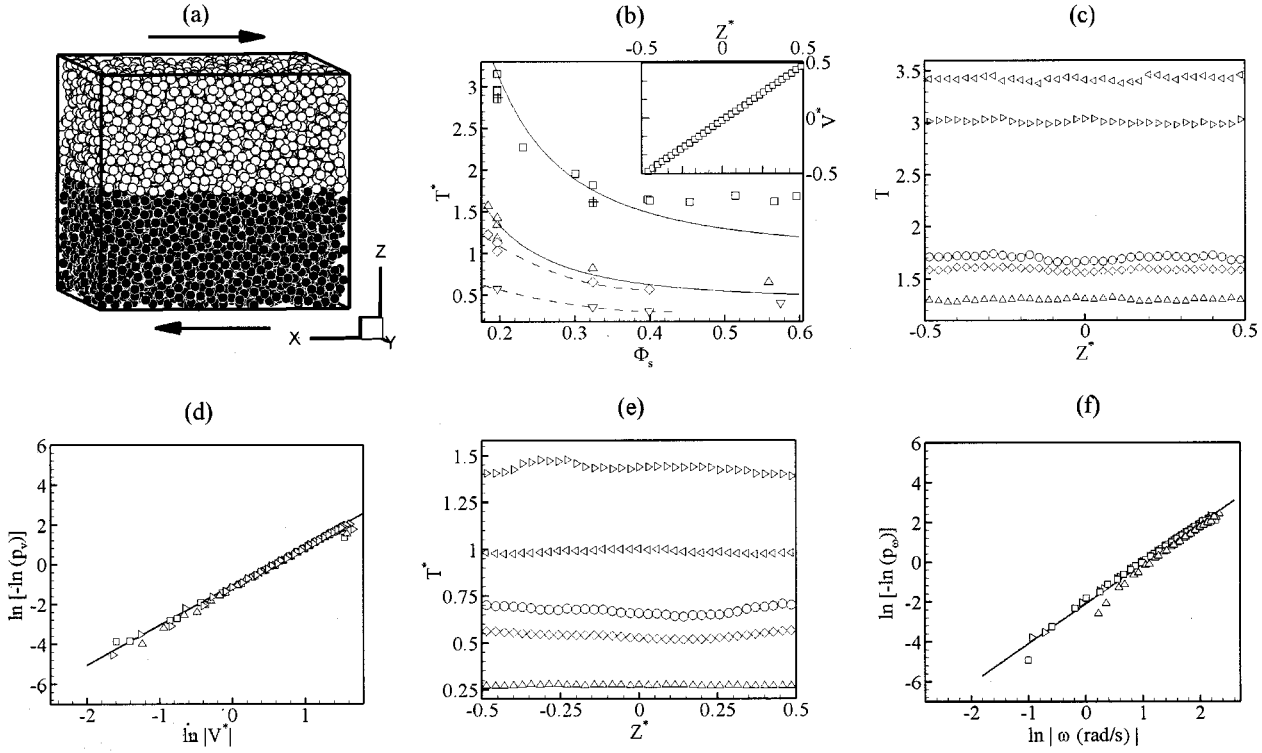

FIG. 2. (a) Side view of a cubic box containing about 10 000 identical nonoverlapping spherical particles, half light and half dark. Arrows show the direction of motion of the wall particles. (b) Dimensionless translational granular temperature T^* as a function of solid fraction. Smooth particles are represented by triangles and squares for $e_0=0.84$ and 0.93, respectively. Squares with plus represent T^* for $e=0.93$, where the coefficient of restitution is assumed to be constant. The upper and lower solid lines represent kinetic theory fits for $e_0=0.93$ and 0.84. For rough particles, inverted triangles are for $e_0=0.84$, $\mu=0.41$, and $\beta_0=0$ and diamonds are for $e_0=0.93$, $\mu=0.123$, and $\beta_0=0.4$. The dashed lines are visual fits through the data. Inset: Distribution of dimensionless velocity as a function of dimensionless distance in z direction. (c) Dimensionless translational granular temperature for smooth particles as a function of dimensionless distance in z direction. Left and right triangles are T_x^* and T_z^* at $\Phi_s\approx 0.2$ and $e_0=0.93$, circles and diamonds are T_x^* and T_z^* at $\Phi_s\approx 0.45$ and $e_0=0.93$, triangles are T_z^* at $\Phi_s\approx 0.2$ and $e_0=0.84$. (d) Graphs of the normalized probability density distributions p_ν for ν_x^*, ν_y^*, ν_z^*, in the form of $\ln[-\ln(p_\nu)]$ versus $\ln(|V^*|)$, where $p_\nu=p(V^*)/p(0)$, at $\Phi_s\approx 0.4$ and $e_0=0.93$. Triangles are for ν_x^*, squares for ν_y^*, and inverted triangles for ν_z^*. The solid line indicates the fitted value for the angular coefficient, which is about 2. (e) Dimensionless translational granular temperature for rough particles as a function of dimensionless distance in z direction. Right and left triangles are T_x^* and T_z^* at $\Phi_s\approx 0.2$ and $e_0=0.93$, $\mu=0.123$, and $\beta_0=0.4$, respectively; circles and diamonds are T_x^* and T_z^* at $\Phi_s\approx 0.4$ and $e_0=0.93$, $\mu=0.123$, and $\beta_0=0.4$, respectively; triangles are T_z^* at $\Phi_s\approx 0.4$ and $e_0=0.84$, $\mu=0.41$, and $\beta_0=0$. (f) Graphs of the normalized probability density distributions p_ω for spins in the form of $\ln[-\ln(p_\omega)]$ versus $\ln(|\omega|)$, where $p_\omega=p(\omega)/p(0)$, at $\Phi_s\approx 0.4$ and $e_0=0.93$, $\mu=0.123$ and $\beta_0=0.4$. The triangles are for ω_x, squares are for ω_y, and inverted triangles are for ω_z. The solid line indicates the fitted value for the angular coefficient, which is about 2. The data of ω_y, which has the mean value of 1.01 s^{-1}, was manipulated to obtain data with zero mean.

Young's modulus; δ_{ij} is the amount of overlap defined as $\sigma-|\mathbf{r}_{ij}|$ and $\mathbf{r}_{ij}$ is the vector connecting the center of mass of particle i to the center of mass of particle j.

A considerable part of the initial kinetic energy does not contribute to the kinetic energy of recoil and is transformed into losses such as the thermal energy and energy of sound oscillation. This transformation seems to occur during the second stage of impact, namely, after the time of maximum compression of the particles. During this period, the shape of the particles undergoes restitution due to the action of the elastic forces, and the potential energy of deformation is again transformed into the kinetic energy. At the end of the second period, the particles are no longer in contact, and their recoil velocities are reduced after impact.

Gugan suggested that Hertz's equations give reasonable results for inelastic collisions even when the energy loss is large [40]. However, Haff [10] argued that for many applications the aforementioned contact scenario is not realized and plastic flow, spallation, cracking, or fracture may occur. By considering the fact that the constituent particles are hard and the amount of deformation near the contact zone is small compared to particle size, Haff suggested a simplified model [10], which might capture the most important contact properties. In this model for a binary collision between i and j particles, the normal contact force is given by [2,10]

$$\mathbf{F}_{n,ij}=\left(k_n\delta_{ij}+\frac{1}{2}m\gamma_n\dot{\boldsymbol{\delta}}_{ij}\cdot\hat{\mathbf{k}}\right)\hat{\mathbf{k}}. \tag{12}$$

In the above equation, $\hat{\mathbf{k}}$ is the unit vector directed from the center of particle i to that of particle j at impact, $\dot{\boldsymbol{\delta}}_{ij}$ repre-

sents the rate of change of $\mathbf{r}_{ij}$, $k_n=(2\times10^5)mg/\sigma$ is the stiffness of a spring that prevents the particles from interpenetrating [2], and γ_n is a constant which accounts for the energy lost at contact due to inelastic processes. Thompson and Grest [2] suggested that the coefficient of restitution e may be defined as $\exp(-\frac{1}{2}\gamma_n t_{\mathrm{col}})$. Here t_{col} represents the contact time, which is a constant defined as $\pi(2k_n/m-\gamma_n^2/4)^{-1/2}$ [2]. However, the measurements [34,40,42] suggested that t_{col} appears to have a characteristic dependence on the impact velocity, namely, $t_{\mathrm{col}}\sim|\mathbf{V}_{ij}^{\mathrm{imp}}|^{-1/5}$.

During the collision of two slipping particles each particle may be subjected to a tangential frictional force that opposes its rotational motion. The tangential force that characterizes the frictional effects may be given by the Coulomb equation

$$\mathbf{F}_{t,ij}=-\mu|\mathbf{F}_{n,ij}|\hat{\mathbf{k}}\times\left(\frac{\mathbf{V}_{ij}^{\mathrm{imp}}}{V_{ij}}\times\hat{\mathbf{k}}\right). \tag{13}$$

For nonslipping contact, Thompson and Grest [2] suggested that the tangential force may be estimated using a different expression,

$$\mathbf{F}_{t,ij}=-\tfrac{1}{2}\gamma_s m\hat{\mathbf{k}}\times(\mathbf{V}_{ij}^{\mathrm{imp}}\times\hat{\mathbf{k}}), \tag{14}$$

where γ_s represents a tangential viscous damping constant. The tangential coefficient of restitution, β, discussed earlier is defined as $\exp(-\gamma_s t_{\mathrm{col}})$ [2].

III. PARTICLE DIFFUSIVITY IN UNBOUNDED SHEAR FLOWS

To simulate an unbounded system of spherical particles subjected to a uniform shear, which is characterized by a velocity gradient of the form $\mathbf{V}(z)=\dot{\varepsilon}z\mathbf{e}_x$, the Lees-Edwards-type [43] periodic boundary conditions were applied to the bounding top and bottom faces of the cubic computational box. Simple periodic boundary conditions [36] were applied on other faces of the computational box. Figure 2(a) illustrates the initial configurations for the simulations. About 10 000 identical nonoverlapping spherical particles, consisting of two species differing only by a color label, were placed randomly in the computational box. The initial velocity of each particle in the x direction was assigned with a magnitude according to a linear velocity profile $\mathbf{V}(z)$ plus a small random number within the interval $[-0.05|\mathbf{V}(L_z)|,+0.05|\mathbf{V}(L_z)|]$. The initial velocities in the y and z directions as well as the spins were all set to zero. Here L_z is the height of the box, and $\mathbf{e}_x$ represents the unit vector in the x direction, which is the direction of mean flow. For the geometry shown in Fig. 2(a), L_z is set to unity.

Simple shear flows

To simulate an unbounded shear flow of a highly idealized system whose dynamics is dominated by collisions, the hard-sphere model discussed in the preceding section is used, for which the particle surface friction μ is set to zero. In this case, the particle surface is characterized only by a coefficient of restitution of e. In the simulations, the solid fraction varied from 0.16 to 0.58. In order to obtain the local description of quantities such as solids fraction, granular temperature, and velocity, first the box is divided into an appropriate number of layers in the z direction, using the criteria suggested by Loose and Ciccotti [44]. Then, the local values are calculated as averages over the particles in the particular layers. Finally, the local values are averaged for 200 configurations each separated by $t^*\approx10^{-2}$. Here, the dimensionless time t^* is defined as $t\dot{\varepsilon}$.

Figure 2(b) illustrates that as the solid fraction in the computational box increases, the dimensionless translational granular temperature $T^*=T/(\dot{\varepsilon}\sigma)^2$ decreases. Figure 2(b) also compares the simulation results for two different values of e_0, namely, 0.93 and 0.84. As expected, the results show that as thermal dissipation increases, the average fluctuation energy of the particles decreases. The results from the hard-sphere model can be compared to those predicted by the kinetic theory analysis for smooth spherical particles, as depicted by a solid line in Fig. 2(b). Note that an expression for T^* may be derived from the kinetic theory of unbounded rapid granular flows [25] by assuming an isotropic distribution of collision angles between the colliding particles:

$$T^*=\frac{1}{24\Phi_s(e_0^2-1)g_c}\left\{\frac{[1+\frac{4}{5}\Phi_s g_c(1+e_0)][\frac{5}{2}+\Phi_s g_c(3e_0^2+2e_0-1)]\pi}{6\Phi_s g_c(1+e_0)(e_0-3)}-\frac{8}{5}(1+e_0)\Phi_s g_c\right\}, \tag{15}$$

where $g_c=[1-(\Phi_s/\Phi_m)^{4\Phi_m/3}]^{-1}$ is the contact value of the equilibrium radial distribution function [45] and Φ_m is the maximum shearable solid fraction for the particles [46]. As can be seen from Fig. 2(b), at higher solid fractions, the dimensionless translational granular temperatures produced by numerical simulations exceed the values of those calculated from the kinetic theory expression (15).

To verify the accuracy of the algorithm, two extra runs were performed, in which the coefficient of restitution was assumed to be independent of the magnitude of impact velocity and was set to a constant value of $e=0.93$. The results from these runs are marked by the squares with plus signs in Fig. 2(b). As can be seen, the translational granular temperatures were slightly lower in these cases, compared to the temperatures calculated for similar cases in which the coefficient of restitution depends on the magnitude of impact

velocity, namely, $e=1-(1-0.93)V_n^{*1/5}$, where setting $V_n^*=V_n/V_0$ to $2V_n$ gives a reasonable fit to the available data. This observation implies that the algorithm is correctly calculating the coefficient of restitution, which is higher than 0.93 for cases in which the impact velocity is lower than the reference velocity in Eq. (2).

Since the number of collisions for which V_n is lower than V_0 increases with the increasing solid fraction, the simulation results for dimensionless granular temperature would be expected to be higher than the calculated values using the kinetic theory expression (15).

Simulations were then performed using a system of inelastic rough spheres subjected to steady shear. The initial configuration is that shown in Fig. 2(a), and the solid fraction again varied from 0.16 to 0.58. Two different sets of values for the surface parameters e and μ were used. The first set was that suggested by Lun and Bent [12] for steel pucks, namely, $e_0=0.93$ and $\mu=0.123$. In this case of sticking binary collisions, β_0 is set to 0.4. The second set was that suggested by Drake [47] for glass beads, namely, $e_0=0.84$ and $\mu=0.41$, with β_0 taken to be zero. A comparison between the results of inelastic, rough particles and those of smooth particles, as shown in Fig. 2(b), indicates that at the same solid fraction, shear rate, and restitution coefficient, the frictional grains are cooler than the frictionless grains.

Figure 2(c) plots the variations of local dimensionless translational granular temperature in longitudinal and lateral directions in the direction of the velocity gradient (namely, the z direction). The nearly flat profiles in Fig. 2(c) are characteristic of unbounded simple shear flows with small amplitude local fluctuations. Moreover, the distributions of dimensionless fluctuation velocities, ν_x^*, ν_y^*, ν_z^*, are Gaussian with standard deviations, $T_x^{*1/2}$, $T_y^{*1/2}$, $T_z^{*1/2}$, respectively, about the mean value zero as shown in Fig. 2(d). Here, the dimensionless fluctuation velocity is defined as $\mathbf{v}^*=\mathbf{v}/\sigma\dot{\varepsilon}$. A comparison between results of the numerical simulations for T^* in the longitudinal direction, namely, T_x^*, and those associated with the lateral directions, namely, T_y^* and T_z^*, as depicted in Fig. 2(c), suggests that the translational granular temperature is not isotropic in simple shear flows of a granular assembly. As shown in Fig. 2(e), the translational granular temperature profiles are also flat, implying that similar behavior exists for unbounded simple shear flows of rough and smooth grains. Moreover, there is no effect of particle roughness on the form of velocity profile. It can be seen from Figs. 2(c) and 2(e) that the ratio of the dimensionless translational temperature of smooth steel balls and rough steel pucks, $T^*_{zsmooth}/T^*_{zrough}$ could be as large as 3 at a solid fraction of $\Phi_s\approx 0.4$. Therefore, the difference in translational temperatures suggests that shearing of the rough particles induces rotational motion. It should be noted that for both of the aforementioned systems the initial values of all spins were set to zero. The evidence for generation of rotational motion in the shearing motion of an assembly of rough particles is illustrated in Fig. 2(f), which presents the probability density distribution of particle spins for a configuration of particles with the surface parameters of $e_0=0.93$, $\mu=0.123$, and $\beta_0=0.4$ at the shear rate of 2 s^{-1}, taken after 2×10^8 collisions.

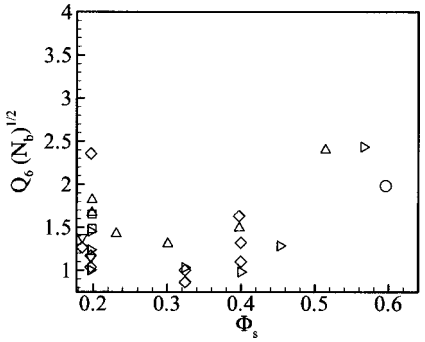

FIG. 3. Variation of $Q_6\sqrt{N_b}$ with solid fraction for both smooth and rough particles. Note that $Q_6\sqrt{N_b}$ for a finite spatially uncorrelated system is ≈ 1.

Note that in this case the shearing motion in the x direction induces a mean rotational motion in the y direction of $\overline{\boldsymbol{\omega}}_y\approx -1.01\mathbf{e}_y$ s^{-1}. Here, $\mathbf{e}_y$ represents the unit vector in the y direction.

Assuming that the particles are uniform solid spheres, the rotational temperature is defined as $\Theta=(\kappa\sigma^2/12N)\Sigma_{i=1}^N[(\omega_{ix}-\overline{\omega}_x)^2+(\omega_{iy}-\overline{\omega}_y)^2+(\omega_{iz}-\overline{\omega}_z)^2]$, where $\overline{\omega}_x=1/N\Sigma_i\omega_{ix}$, $\overline{\omega}_y=1/N\Sigma_i\omega_{iy}$ and $\overline{\omega}_z=1/N\Sigma_i\omega_{iz}$ are the average values of the spins in the x, y, and z direction, respectively. Here N represents the total number of particles in the computational box. The dimensionless rotational temperature in the direction of the velocity gradient may be defined as $\Theta_z^*=\kappa\Sigma_i(\omega_{iz}-\overline{\omega}_z)^2/(4N\dot{\varepsilon}^2)$. As seen in Fig. 2(f), a normal distribution with zero mean and variance of 3.75, which is shown by a solid line, provides good approximations for spins in the z direction. Using $\kappa=\frac{2}{5}$ for a uniform solid sphere, Θ_z^* for the aforementioned case was found to be close to 0.1. In this case, the difference in total (rotational plus translational) fluctuation energy of the systems of rough and smooth particles could be due to the fact that in the system of rough particles, the dissipation into thermal energy occurs by means of both friction and inelastic collisions.

To investigate the signature of order in the sheared granular system, the variation of $Q_6\sqrt{N_b}$ (instead of Q_6) as a function of solid fraction for both smooth and rough particles is given in Fig. 3. As mentioned earlier, $Q_6\sqrt{N_b}\approx 1$ for a spatially uncorrelated system. Using this normalized value the effect of having different number of bonds for different samplings can be removed. As $Q_6\sqrt{N_b}$ approaches 2.5, there is still significant disorder in the system. Note that the value of $Q_6\sqrt{N_b}$ for a system with cuboctahedral symmetry could be even higher than 100. Hence, the structural changes that occur during the process of increasing the solid fraction are small and the system remains disordered even at high solid fractions. This indicates that as the solid fraction is further increased the grains may become frozen and a noncrystalline solid (namely, a glass) may form. An increased understanding of the glass transition could provide insight into the dynamics of spatiotemporal fluctuations in a dense slowly evolving granular system. Unfortunately, computer simulation results such as those presented here may provide only limited insight, since hard-sphere models may not be adequate to capture cooperative motion, such as the rearrange-

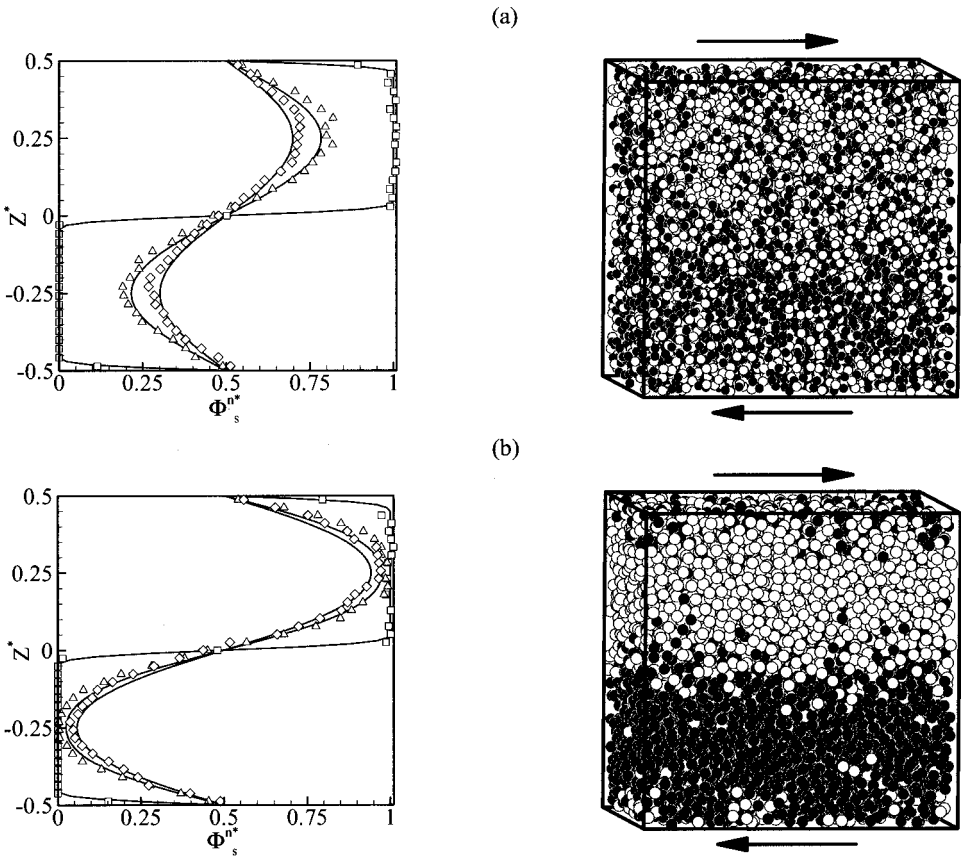

FIG. 4. (a) Left: Variations of a normalized solids fraction of light particles as a function of dimensionless distance in the z direction at different dimensionless times t^*. Squares are at $t^*=0$, left triangles are at $t^*=30$, circles are at $t^*=39$. The total solids fraction is $\Phi_s \approx 0.2$ and $e_0=0.93$. The solid lines represent analytical solutions (18) for which T_z^* is given in Fig. 2(c) (right triangles) and $\sigma^* \approx 0.034$. (a) Right: Mixing of light and dark particles in the computational box at $t^*=39$. (b) Left: Variations of a dimensionless solids fraction of light particles as a function of dimensionless distance in the z direction at different dimensionless times t^*. Squares are at $t^*=0$; left triangles are at $t^*=30$; circles are at $t^*=39$. The total solids fraction is $\Phi_s=0.45$ and $e_0=0.93$. The solid lines represent analytical solutions (18) for which T_z^* is given in Fig. 2(c) (diamonds) and $\sigma^*=0.043$. (b) Right: Mixing of light and dark particles in the computational box at $t^*=39$.

ment of clusters of grains, which seems to dominate structural relaxation at high solid fractions.

In sheared granular fluids where the interactions between the grains lead to correlations between the positions and velocities of different grains, the self-diffusion may be interpreted as a result of cooperative effects of macroscopic solid fraction fluctuations. Thus an analysis of particle diffusive motion may contribute to the understanding of issues such as cooperative motion in a granular fluid. To this end, shear-induced dispersions of grains in the z direction at solid fractions of $\Phi_s \approx 0.2$ and 0.4 are illustrated in Fig. 4. The side view of grains in the system before application of strain in the x direction is shown in Fig. 2(a). As shown in Fig. 4, as time evolves, light grains migrate away from the upper region, causing their solid fraction to decay from its initial profile, with a higher rate of mixing for lower values of total solid fraction.

To investigate the mixing behavior as shown in Fig. 4, a diffusion law may be obtained by assuming that the random-walk-type displacements of grains in the z direction are not coupled to these in any other directions. Thus, a dimensionless mass balance for the light particles may be given by [25]

$$\frac{\partial \Phi^{l*}}{\partial t^*} - D_z^* \sigma^{*2} \frac{\partial^2 \Phi^{l*}}{\partial z^{*2}} = 0. \tag{16}$$

In the above equation, $z^*=z/L_z$, $\Phi_l^*=\Phi_l/\Phi_s$, $D_z^*=D_z/\sigma^2\dot{\varepsilon}=\pi^{1/2}T_z^{*1/2}/[8(1+e_0)\Phi_s g_c]$, $\sigma^*=\sigma/L_z$, and Φ_s represents the total solid fractions of light and dark particles. Here, the expression for the diffusion coefficient in the z direction is given by $D_z=\sigma\pi^{1/2}T_z^{1/2}/[8(1+e_0)\Phi_s g_c]$, which may be derived from the kinetic theory of unbounded rapid granular flows [25]. The system shown in Fig. 2(a) is subject to the three conditions

$$\begin{aligned} &t^*=0, \quad \begin{cases} z^*>0, & \Phi_l^*=1 \\ z^*<0, & \Phi_l^*=0, \end{cases} \\ &t^*>0, \quad z^*=\tfrac{1}{2}, \quad \Phi_l^*=\tfrac{1}{2}, \\ &t^*>0, \quad z^*=\tfrac{1}{4}, \quad \frac{\partial \Phi_l^*}{\partial z^*}=0. \end{aligned} \tag{17}$$

The solution to this problem is given by [48]

$$\begin{aligned} \Phi_l(t^*,z^*) = \frac{1}{2} + \sum_{n=1}^{\infty} e^{-\pi^{5/2} n^2 \sigma^{*2} T_z^{*1/2} t^*/2(1+e_0)\Phi_s g_c} \\ \times \left[\frac{\sin(n\pi)}{n\pi} \cos(2n\pi z^*) \right. \\ \left. + \frac{1-\cos(n\pi)}{n\pi} \sin(2n\pi z^*) \right]. \end{aligned} \tag{18}$$

A comparison between the analytically obtained solid fraction distributions (18) and those obtained from numerical simulations, which are shown by symbols in Fig. 4, suggests that in the range of solid fractions given above, the grain

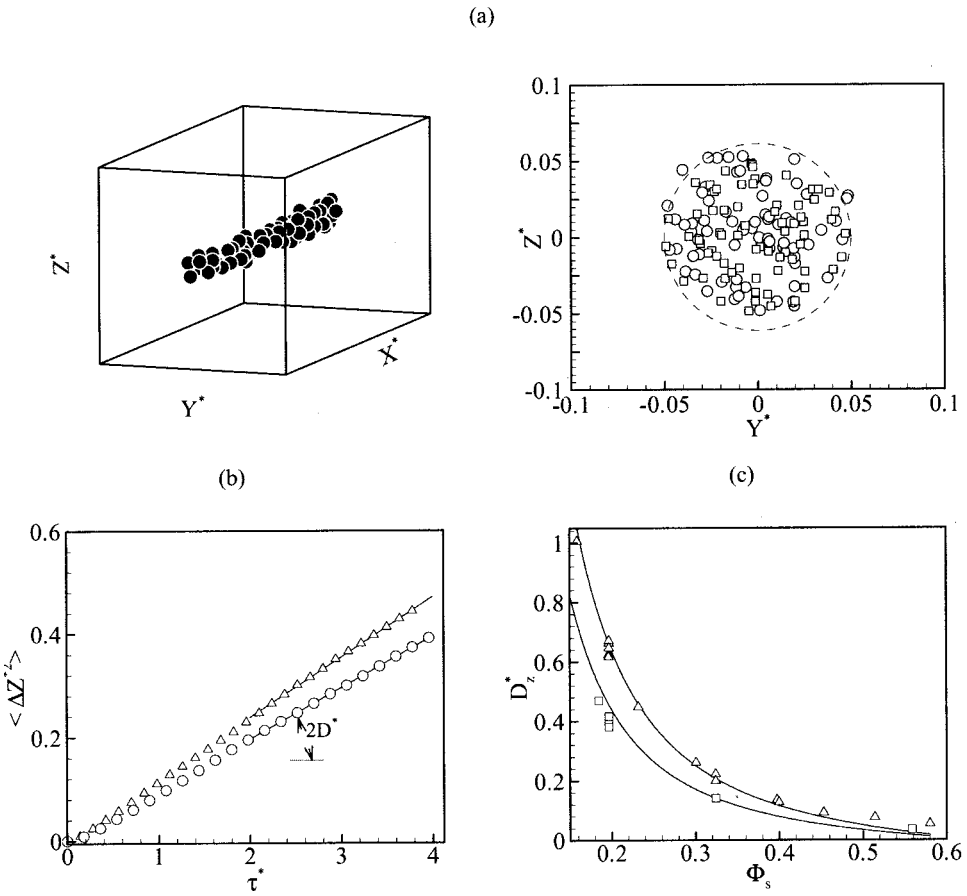

FIG. 5. (a) Left: Initial configuration of tracer grains in the computational box. (a) Right: Dispersion of the grains. Squares are initial positions and circles are positions of grains after a short period of time in a dimensionless *yz* plane. (b) Variations of $\langle \Delta z^{*2} \rangle$ with the dimensionless delay time τ^* at $\Phi_s = 0.565$ for the smooth particles in an unbounded shear flow. Triangles and circles are $e_0 = 0.84$ and $e_0 = 0.93$, respectively. The solid lines represent linear fits, with slopes of $2D_z^*$. (c) D_z^* as a function of solid fraction. Squares are $e_0 = 0.84$, triangles are $e_0 = 0.93$. The upper and lower solid lines are the kinetic theory results, namely, $D_z^* = \pi^{1/2} T_z^{*1/2} / [8(1+e_0)\Phi_s g_c]$, with the values of T_z^* given in Fig. 2(c), for $e_0 = 0.93$, 0.84.

displacements in the z direction are of random walk type characterized by a self-diffusion coefficient D_z.

To make the preceding remarks more specific, suppose that N_0 is the number of tracer grains initially situated about $Z=0$ in the computational box, as shown in Fig. 5(a). To obtain a better visualization, the normal grains have not been shown in this figure. Due to shearing motion at time $t>0$, the tracers are spatially dispersed about $Z=0$. The evidence of dispersion is illustrated in Fig. 5(a), which shows the positions of tracer grains in a *yz* plane taken at two different times. At any time $t>0$ the second moment of the number of tracers per unit volume, $N(z,t)$, represents the mean-square displacement of the traces in the z direction. That is, $\langle [z(t) - z(0)]^2 \rangle = (1/N_0) \int z^2 N(z,t) dz$. If the tracers are spatially distributed in a Gaussian such as $N(z,t) = N_0 / (2\sqrt{\pi D t}) \exp[-z^2/(4Dt)]$, then the self-diffusion coefficient is given by [19]

$$D = \frac{\langle [Z(t) - Z(0)]^2 \rangle}{2t} = \frac{\langle \Delta Z^2 \rangle}{2t}. \tag{19}$$

Equation (19) applies when the time t is large compared to the average time between collisions of grains. Here the angular brackets denote the ensemble average and the samples are taken at time intervals τ apart.

Figure 5(b) illustrates the variations of the dimensionless mean-square displacement in the z direction with the dimensionless delay time $\tau^* = \tau\dot{\varepsilon}$ at $\Phi_s = 0.56$ for smooth particles with surface parameters $e_0 = 0.84$ and $\mu = 0$. The displacements were evaluated excluding periodic boundary conditions. At long times where the deviation from the free diffusion regime becomes apparent, $\langle \Delta Z^2 \rangle$ behaves linearly in t. This observation may suggest that the linear Fick's law describes, on average, the dissipation of spontaneous microscopic density fluctuations. In this case the dimensionless diffusion coefficient in the direction of the velocity gradient is found to be $D_z^* = 0.05$, which is close to that measured by Bridgwater [18] in the simple shear apparatus, namely, 0.057. Note that the solids fraction was not reported in [18]. As also seen in Fig. 5(b), at a solid fraction of 0.56, using the values $e_0 = 0.93$ and $\mu = 0$ for the surface parameters in the simulation results in $D_z^* = 0.059$. The dimensionless translational temperature in the direction of the velocity gradient, T_z^*, for this case is found to be 1.62. Considering the dimensionless diffusion coefficients D_z^* given in Fig. 5(b), along with a comparison between the corresponding translational temperatures T_z^*, it appears that the diffusive motion of particles is mainly controlled by the translational temperature, whose value is a function of the coefficient of restitution, e. The results also indicate that e can be adjusted to obtain the value of the dimensionless transverse diffusion coefficient measured by Bridgwater [18], which was 0.057. Perhaps a reasonable value for the coefficient of restitution describing the surface properties of phenolic resin balls would be in the range $0.84 \leqslant e \leqslant 0.93$, but closer to the higher end of the range.

Figure 5(c) compares the theoretical results obtained using $D_z^* = \pi^{1/2} T_z^{*1/2} / [8(1+e_0)\Phi_s g_c]$ with those predicted by

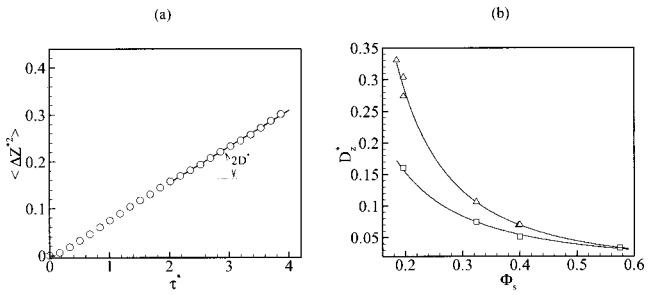

FIG. 6. (a) Variation of $\langle \Delta z^{*2} \rangle$ as a function of dimensionless delay time τ^* at $\Phi_s = 0.565$ and the surface parameters $e_0 = 0.84$, $\mu = 0.41$, and $\beta_0 = 0$. The solid line represents a linear fit. T_z^* and D_z^* are 0.348, 0.038. (b) D_z^* as a function of solid fraction. The squares are $e_0 = 0.84$, $\mu = 0.41$, and $\beta_0 = 0$; triangles are $e_0 = 0.93$, $\mu = 0.123$, and $\beta_0 = 0.4$.

the simulations at two different coefficients of restitution. It can be seen that the aforementioned expression for D_z^* reasonably fits the numerical results for systems with a solid fraction lower than 0.45. However, the simulation results exceed the theoretical value at higher solid fractions. In the present simulations, Eq. (2) was used to describe the inelastic behavior of the grains. Therefore, it is not clear whether the deviations may be attributed to an enhancement of the velocity correlations due to the excitation of slowly decaying cooperative motions in a dense granular fluid, or to the use of different expressions for the coefficient of restitution in the simulations and the kinetic theory expression.

The presence of long-duration frictional contact between particles was reported by Natarajan, Hunt, and Taylor [21]. It may be speculated that in their gravity driven flow, the gravitational effects contribute insignificantly to the particle diffusive motion in the direction of the velocity gradient, which is perpendicular to the direction of gravity. The obtained value of the dimensionless diffusion coefficient D_z^*, for the present simulations of a system of frictionless grains, is somewhat larger than the values of the dimensionless lateral diffusion coefficient measured in the moderately low shear region in the experiments [21], which was 0.0397. Recall that at the extremely high average solid fraction of $\Phi_s > 0.6$, a difference of four orders of magnitude exists between the values of dimensionless diffusivity in the direction perpendicular to the main flow, measured by Menon and Durian [8], and that calculated from the results of Natarajan, Hunt, and Taylor [21]. Assuming that the solid fraction in the latter case was much lower than that in the former case, it may be concluded that the value of D_z^* falls below its theoretical value at solid fractions close to the glass transition.

Figure 6(a) plots the variations of the dimensionless mean-square displacement of rough particles in the z direction, $\langle \Delta z^{*2} \rangle = \langle \Delta z^2 \rangle / \sigma^2$, with a dimensionless delay time τ^*, a shear rate $\dot{\varepsilon} = 4\ \mathrm{s}^{-1}$, a solid fraction of $\Phi_s = 0.565$, and surface parameters of the second set mentioned above, namely, for glass particles. After 10^7 collisions, it was found that the value of the dimensionless diffusion coefficient did not depend on the choice of time origin, which indicates that the system had attained a steady state. As shown in Fig. 6(a), at long times $\langle \Delta z^{*2} \rangle$ behaves linearly in τ^*, which may justify the use of the Einstein formula for calculating the macroscopic dimensionless diffusion coefficient in the direction of velocity gradient. From Fig. 6(a) it is found that $D_z^* = 0.0394$. This value does not vary with the shear rate. In the present cases, the average dimensionless translational temperature T_z^* is found to be 0.352. Therefore, it can be concluded that for these cases, the translational temperature in the direction of the velocity gradient, T_z, was quadratically dependent on the shear rate. The obtained value of the dimensionless diffusion coefficient D_z^* for the present simulations is very close to the average of the values measured in the moderately low shear region in the experiments [21], which was 0.0397. This agreement, which supports the earlier conjecture that the particle diffusive motion in their system is governed by shearing motion and that the effect of gravity could be of minor relevance, is quite impressive. Moreover, this finding may also suggest the value of solid fractions in the experiments [21].

It is worth mentioning that at the same solid fraction and shear rate, particles with smooth surfaces tended to show more diffusive motion in the direction of the velocity gradient than particles with rough surfaces. Comparing the results in Figs. 5(c) and 6(b), the dimensionless diffusion coefficient D_z^* of the smooth particles is greater by a factor of about 1.5 than that of the rough particles. An explanation for the difference in the dimensionless diffusion coefficient is suggested by the observation that the dimensionless translational temperature in the direction of the velocity gradient of the rough particles is lower than that of the smooth particles.

In the absence of any theoretical treatment for predicting the diffusive motion of rough grains in a sheared flow, the dimensionless lateral diffusive coefficient is extracted from the data using the Einstein formula (21). The results are illustrated in Fig. 6(b), which plots D_z^* as a function of the solid fraction. The dimensionless lateral diffusion coefficient for rough grains is smaller than that for smooth grains at a given value of the solid fraction. However, the present results do not seem to indicate at what solid fraction the transition to the glass state occurs.

Haff [10] suggested that hard-sphere models suffer from several limitations including the lack of a realistic model for the contact forces between grains. Thus, the use of hard-sphere models may not be justified when the solid fraction is very high and the particle free times are shorter than the duration of the contacts. A related question can then be posed regarding the extent to which a true model for the contact forces between the grains affects the simulation results for an assembly of uniform grains subjected to a shearing deformation. In the present simulations it is important to note that the probability of finding free times shorter than 10^{-4} s is quite rare even at a solid fraction of 0.58 for smooth particles, as illustrated in Fig. 7(a). According to the classical theory of impact between frictionless elastic bodies [41], the total duration of collision, T_c, of two identical spherical particles with mass m, diameter σ, and elastic coefficient χ, is given by $T_c = 4.347[m\chi/\sigma^{1/2}]^{2/5} V_n^{-1/5}$. Thus T_c could be as small as 8×10^{-5} s for phenolic resin particles with diameters of 18.6 mm used in [18] having the normal impact velocity of

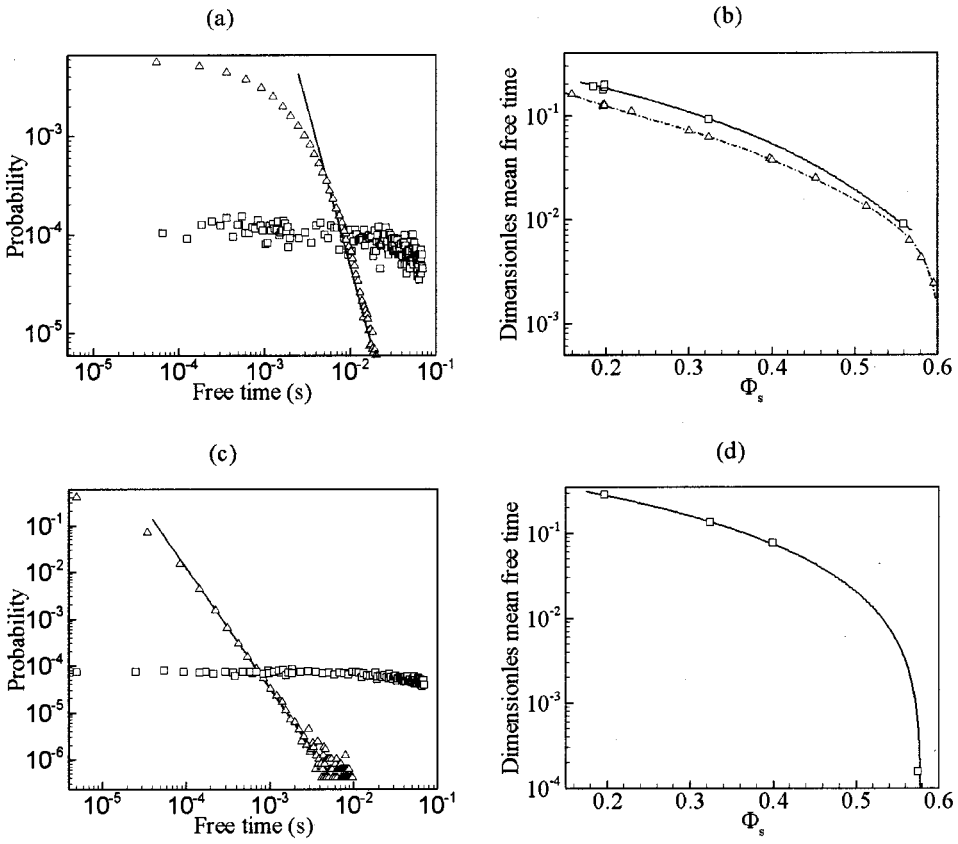

FIG. 7. (a) Probability of particle free time for two different solid fractions for $e_0=0.93$. The squares are $\Phi_s \approx 0.2$, triangles are $\Phi_s \approx 0.56$. The straight line indicates the power law τ^{-3}. (b) Dimensionless mean free time as a function of solid fraction. The squares are $e_0=0.84$, triangles are $e_0=0.93$. (c) Probability of particle free time for two different solid fractions for the surface parameters $e_0=0.84$, $\mu=0.41$, and $\beta_0=0$. The squares are $\Phi_s \approx 0.2$, triangles are $\Phi_s \approx 0.57$. The straight line indicates the power law $\tau^{-2.6}$. (d) Dimensionless mean free time as a function of solid fraction for $e_0=0.84$, $\mu=0.41$, and $\beta_0=0$. The solid lines in (b) and (d) are visual fits through the data.

20 cm/s. At the same impact velocity, the value of T_c for 1-mm glass particles is one order of magnitude lower than that for phenolic resin particles. These estimated values for T_c suggest that the hard-sphere model could be of use to illuminate the basic features of the shear flow of granular material even at high solid fractions. The corroborating evidence is the agreement between the numerical results and the measured values for the dimensionless self-diffusion coefficient discussed above.

It is interesting that at the solid fraction of 0.58, the statistics of a time τ during which a particle flies freely between two successive collisions displays a power law distribution, $P(\tau) \sim \tau^{-\alpha}$, with exponent $\alpha \approx 3$. There is a short-time cutoff where the uniform distribution is observed as τ approaches very low values. However, as depicted in Fig. 7(a), which compares the statistics of τ at two different solid fractions, a nearly uniform distribution is observed for the whole range of particle free times at a low solid fraction of 0.2.

Figure 7(b) shows the variations of dimensionless mean free time as a function of solid fraction for smooth particles. At a specified solid fraction, the granular fluid with lower dissipation rate (and thus a higher granular temperature) is observed to have a lower mean free time. Also, the mean free time decreases sharply close to a solid fraction of 0.6, where the glass transition may occur. The condition is even more pronounced in the case of rough particles at very high solid fractions, namely, close to the glass transition solid fraction Φ_g. From Fig. 7(c) it may be concluded that a fairly high probability exists of finding free times shorter than 10^{-4} s at solid fractions higher than 0.58. The results show that the statistics of free time τ displays a power law distribution, $P(\tau) \sim \tau^{-\alpha}$, with exponent $\alpha \approx 2.6$, and there is a very small sign of short-time cutoff where the uniform distribution could be observed as τ approaches very low values. As shown in Fig. 7(c), which compares the statistics of free time τ at two different solid fractions, a nearly uniform distribution is again observed for the whole range of particle free times at the low solid fraction of 0.2. Figure 7(d) shows the variations of dimensionless mean free time as a function of solid fraction. At very high solid fractions the mean free time rapidly drops to extremely small values. The results presented in Fig. 7 suggest that particle dynamics models should be used to obtain more reliable results at very high solid fractions.

At this stage, it is worthwhile to investigate to what extent the Kelvin-type model of Haff [10] for linear viscoelastic grains at contact mimics the real granular flows. It was suggested that a linear visoelastic behavior is often found at small deformations, and that a model based on this behavior predicts a constant collision time. Recently, Gugan [40] measured the duration of contact, T_c, as a function of normal velocity at impact, V_n, for frictionless balls striking a flat surface. Although the collisions were dissipative, the results for $T_c(V_n)$ are found to be consistent with Hertz's elastic theory of impact. In this light, a model is developed in which the contact of frictionless grains produces a normal repulsive contact force whose magnitude is proportional to the $\frac{3}{2}$ power of the amount of overlap. In this model for a collision be-

TABLE II. A comparison between results for contact time from measurements and simulations.

V_n (m/s)	Values measured [40] T_c (ms)	Simulation results T_c (ms)
2.19	0.97	0.97
2.78	0.90	0.93
3.67	0.83	0.88
4.24	0.81	0.85
4.99	0.79	0.83
5.50	0.79	0.81

tween a ball and a flat surface, the normal contact force during a collision is given by $\mathbf{F}_n=(K_n\delta^{3/2}+G_n\dot{\boldsymbol{\delta}}\cdot\hat{\mathbf{k}})\hat{\mathbf{k}}$, where G_n represents the dynamic damping, which is a measure of the energy loss at contact due to inelastic processes. Here G_n is a function of the impact velocity, which is calculated using the e-V_n relationship given in [40].

As given in Table II, using the nonlinear model the simulation results for T_c are found to be in good agreement with measured values [40]. The predicted collision times are not constant, but are a function of velocity at impact. Moreover, the coefficient of restitution decreases from unity as the normal impact velocity increases from zero, in qualitative agreement with the results given in [34,42,49]. For most solid substances, the coefficient of restitution, e, is a function of impact velocity V_n. Thus the primary issue regarding the models for the contact forces between grains is how closely the model can predict the e-V_n relationship. Limited information is available for the e-V_n relationship for solid substances [34,42,49].

The present results highlight the limitation of the particle dynamics model for linear viscoelastic grains [2,9,10], which predicts a constant collision time, which results in a constant coefficient of restitution. More limitations of the aforementioned model are evident considering the results presented in Fig. 8. Figure 8(a) shows the variations of the x, y, and z components of the normal contact force as a function of time in a binary collision of two glass beads with diameter 4.8 mm. The impact velocity is selected to be 0.56 m/s and the coefficient of restitution is set to be 0.84. The solid lines indicate the results for linear, viscoelastic, frictionless grains obtained using Eq. (12), whereas those calculated using $\mathbf{F}_{n,ij}=(K_n\delta_{ij}^{3/2}+G_n\dot{\boldsymbol{\delta}}_{ij}\cdot\hat{\mathbf{k}})\hat{\mathbf{k}}$ with $G_n(V_n)=1.36(V_n/V_0)^{1/5}+0.063(V_n/V_0)^{2/5}$ kg/s are shown by a dashed line. Here V_0 represents a reference velocity. A comparison between the results of linear and nonlinear models reveals that the predicted maximum contact force using the nonlinear model is one order of magnitude higher than that found using the linear model. Also a much shorter duration of collision is observed for the nonlinear model. At the same impact velocity, increasing the diameter of glass beads to 48 mm decreases the difference between the maximum contact forces predicted by the models as shown in Fig. 8(b). Moreover, the numerical values for the collision times become closer to each other. Therefore, the differences between the models' predictions are more pronounced when the size of grains becomes smaller. For 48-mm particles a different G_n-V_n relation is used, which is $G_n(V_n)=-52.4(V_n/V_0)^{1/5}+291.4(V_n/V_0)^{2/5}$ kg/s.

To show that even simple shear flows of frictionless grains can produce complex structures even in simple situations, simulations were performed for unbounded flow using about 10 000 glass beads. The diameter of beads is $\sigma=4.8$ mm with the material density of $\rho=2500$ kg/m^3. For the geometry shown in Fig. 2(a), the width, length, and height of the computational box were each selected to be 10 cm. The beads were subjected to a uniform shear, which is characterized by a shear rate of $\dot{\varepsilon}=20\ \mathrm{s}^{-1}$. The solid fraction is close to 0.58. For the linear model, k_n and γ_n are set to 6×10^4 kg/s^2 and 3162 s^{-1}, respectively. These parameters give a constant collision time of 1.1×10^{-4} s (for a binary collision) and a constant coefficient of restitution of 0.84. The second model is the nonlinear viscoelastic model for which a generalized form of the aforementioned nonlinear model is used, by which multiple contacts can be predicted. In this model the damping coefficient is given by $G_n(V_n)=1.36(V_n/V_0)^{1/5}+0.063(V_n/V_0)^{2/5}$ kg/s. The other model parameter that controls the stiffness of the material, namely, K_n, is set to 2.24×10^9 Pa m$^{1/2}$. The equations of motion are integrated using fourth- and fifth-order embedded formulas from Dormand and Prince [50] with $\Delta t\approx t_{\mathrm{col}}/100$.

Both models predict the formation of flattend clusters. However, the nonlinear model predicts a shorter cluster lifetime as compared to the linear model. However, the maximum intraparticle forces are much larger in the nonlinear model. Recall that in the experiments of Miller, O'Hern, and

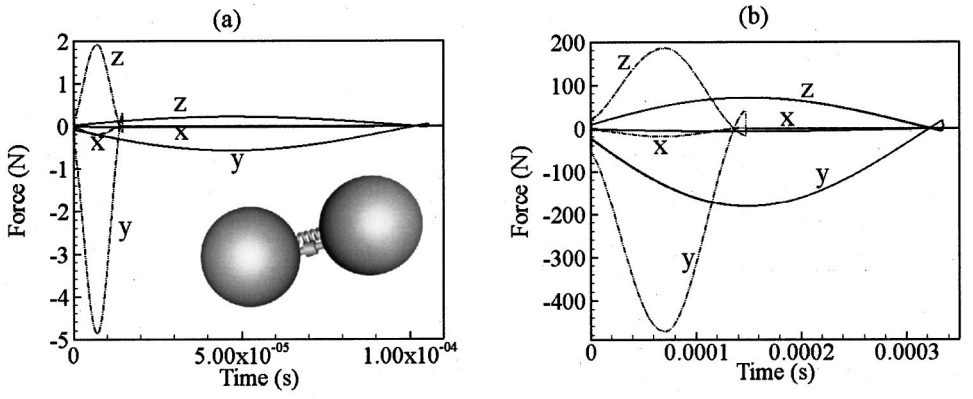

FIG. 8. (a) Variations of forces in the x, y, and z directions as a function of time for 4.8-mm glass beads using linear (solid line) and nonlinear (dashed line) models. Here, X, Y, and Z denote x, y, and z directions. Inset: Schematic of a binary collision of smooth particles for the linear model. (b) Comparison similar to that in (a) for glass beads with a diameter of 48 mm.

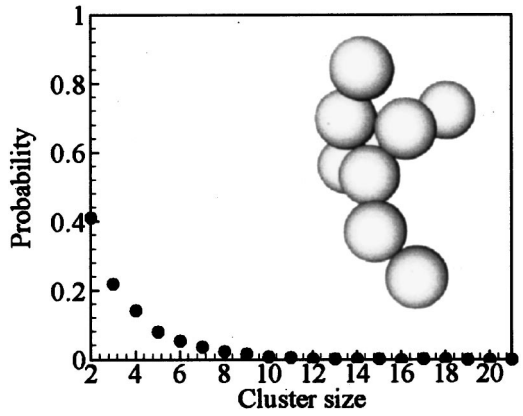

FIG. 9. Instantaneous cluster size probability density distribution in the computational box at $\Phi_s = 0.586$. Inset: A chainlike cluster consisting of eight frictional particles found in the computational box.

Behringer [4], in which 4-mm particles were used, the largest peaks in the normal stress signal were about ten times the average value of the normal stress. This observation appears to be more consistent with the intraparticle forces predicted by the nonlinear model.

In many systems of practical interest the presence of a long-duration frictional contact between grains has been observed [21]. Thus, the importance of surface friction in flow dynamics of sheared granular flows should also be studied. In order to model in a simple way the change of geometrical contacts during collisions of rough grains, the linear model of Thompson and Grest [2] was used. As suggested in [2] the parameters γ_n and γ_s, which ensure that collisions between grains are inelastic, are set as $\gamma_n = 2\gamma_s$, which means that the normal and tangential coefficients of restitution have a value of 0.84. The static Coulomb friction coefficient μ is set to 0.4. In this series of simulations the diameter of beads is $\sigma = 4.76$ mm with the density of $\rho = 2500$ kg/m^3. Again the width, length, and height of the computational box were each selected to be 10 cm and the number of grains in the simulations was 10 187. The grains were subjected to a uniform shear with a shear rate of $\dot{\varepsilon} = 20\ \mathrm{s}^{-1}$. The solid fraction is close to 0.586. Contrary to the flattened clusters using smooth particles, here the structures were found to be more like elongated chains as shown in the inset of Fig. 9.

The nature of the interactions in a dense frictional granular assembly under a shearing motion can be examined by analyzing the formation and disintegration of the chainlike cluster presented in the inset of Fig. 9. Using a linear model, it was found that the effective lifetime of the chain is of order of 10^{-4} s. This result implies that the use of the hard-sphere model, which predicts the mean free time of order 10^{-5} s, may produce an incorrect picture of the complex behavior involved in the rearrangements of the grains at the solid fraction of 0.58. Therefore, questions regarding the heterogeneity and cooperativity of granular dynamics in glasses might be answered only by using a model that treats the contact forces between the grains appropriately.

An important question to consider at this point is to what precision could a linear model as suggested in [2] predict the contact forces between the grains. To address this concern the differences between the linear model [2] and nonlinear model predictions are discussed below. In the nonlinear model, during the contact of grains i and j the former grain feels a force, which is given by

$$\mathbf{F}_{ij} = (K_n \delta_{ij}^{3/2} + G_n(V_n)\dot{\boldsymbol{\delta}}_{ij}\cdot\hat{\mathbf{k}}_{ij})\hat{\mathbf{k}}_{ij} - \left\{\min\left\{\mu\mathbf{F}_{ij}\cdot\hat{\mathbf{k}}_{ij}, G_t(V_n) \times\left[\hat{\mathbf{k}}_{ij}\times\left(\frac{\mathbf{V}_{ij}^{\mathrm{imp}}}{|\mathbf{V}_{ij}^{\mathrm{imp}}|}\times\hat{\mathbf{k}}_{ij}\right)\right]\cdot\mathbf{V}_{ij}^{\mathrm{imp}}\right\}\right\}\left[\hat{\mathbf{k}}_{ij}\times\left(\frac{\mathbf{V}_{ij}^{\mathrm{imp}}}{|\mathbf{V}_{ij}^{\mathrm{imp}}|}\times\hat{\mathbf{k}}_{ij}\right)\right]. \tag{20}$$

Here $G_t(V_n)$ represents the dynamic damping coefficient in the tangential direction, which characterizes the restitution of velocity in the tangential direction for nonslipping contacts. Here it is assumed that $G_t(V_n) = \frac{1}{2}G_n(V_n) = 0.68(V_n/V_0)^{1/5} + 0.0315(V_n/V_0)^{2/5}$ kg/s.

Using a nonlinear model for beads with $\sigma = 4.76$ mm and density $\rho = 2500$ kg/m^3, the effective lifetime of the chain is found to be as short as 3×10^{-5} s, but the maximum intraparticle forces are quite large compared to those predicted by the linear model. Again by considering the measured force fluctuations in [4] it appears that the nonlinear frictional model could predict the interactions of grains in dense granular flows more precisely than a linear model.

Figure 9 illustrates the instantaneous cluster size distribution in a sheared dense granular assembly with a solid fraction of about 0.586 for which particle-particle interactions were modeled using the aforementioned nonlinear model. Surprisingly, the changes in cluster size distribution are small when a linear model was used. However, note that the use of periodic boundary conditions may inhibit the occurrence of larger structures in a computational box whose length is 21 particle diameters.

As discussed above, the ordering of particles as illustrated in Fig. 1 was observed neither in simulations of the unbounded system of particles with rough surfaces nor in those in which the particles were smooth. Therefore, simulations of bounded shear flows of a granular material for which the wall effects are significant are required to investigate the experimentally observed transition to an ordered state.

IV. BOUNDED SHEAR FLOWS

Methods such as photoelasticity [51] can be used to display the contacts between particles in dense bounded shear flows. However, determining the contact duration between particles remains a difficult task. In this context, numerical analysis could provide some guidance. For instance, the analysis of the impact between grains discussed in the preceding section may be useful in calculating the duration of impact in terms of the size, relative velocity of impact, and physical properties of the solid. The obtained results showed that the average duration of an impact in the experimental apparatus of [4] could be about 5×10^{-5} s for glass beads of diameter 4 mm. It was also found that the duration of impact is significantly longer for larger particles. The ratio of the impact duration to the particle mean free time was identified

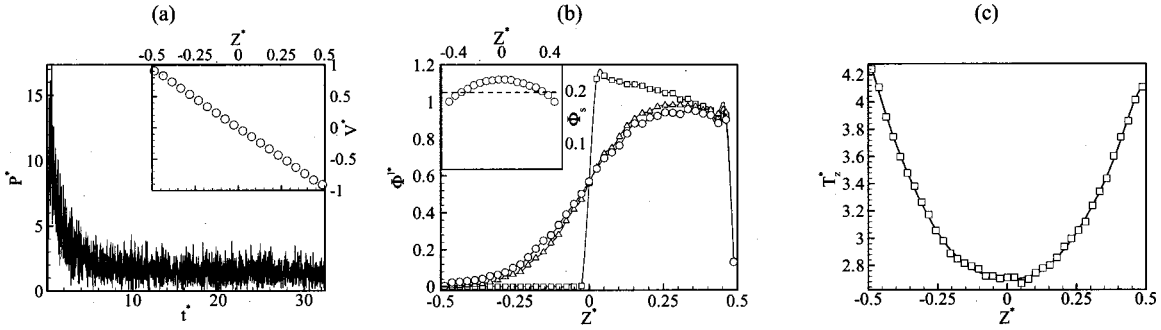

FIG. 10. (a) Dimensionless normal stress P^* exerted on the upper wall versus dimensionless time t^* for smooth particles at $\Phi_s \approx 0.2$ and the apparent shear rate of $\dot{\varepsilon}=2\ \mathrm{s}^{-1}$, for $e_0=0.93$ and $\sigma^* \approx 0.032$. Inset: Distribution of dimensionless velocity as a function of dimensionless distance in z direction. (b) Variations of the normalized solid fraction of light particles as a function of dimensionless distance in the z direction at different dimensionless times t^*. Squares are at $t^*=0$, triangles are at $t^*=24$, circles are at $t^*=33$. The solid lines are visual fits through the data. Inset: Variation of the total solid (light and dark) fraction as a function of dimensionless distance in the z direction. The dashed line represents the average solid fraction. (c) Variations of T_z^* as a function of dimensionless distance in the z direction.

as a criterion for selecting the relevant model for the simulation of sheared granular flows. In this light, a modified hard-sphere model, which is an event-driven algorithm, may not be recommended for a system whose solid fraction is higher than 0.56. For more dense systems, for which the precise information about the rearrangement of grains is essential, a more computationally intensive force-driven algorithm based on the particle dynamics model is recommended.

In this section, simulation results for the hard-sphere model for bounded shear flows at moderately dense and dense solid fractions, for various values of the phenomenological parameters, are compared qualitatively to the results of recent experiments. Moreover, the predictions of this model in the presence of gravity are also included, which could help to distinguish the effects of different factors in the results of the simulation. Then, the rough pictures provided by the hard-sphere models are refined by performing simulations using the particle dynamics model to obtain an increased understanding of dense granular systems, especially their transitions to a solid phase.

A. Fixed volume simulations

For the fixed volume bounded shear simulations, the only modification to the computational box shown in Fig. 2(a) is the introduction of two rough walls with a fixed separation distance, each comprised of an irregular cubic array of 625 massive hemispherical particles with the same diameter as the interior particles. Here, the interior particles are driven into shearing flow by moving the top and bottom walls at a velocity V_{x0} in opposite directions along the x direction. Thus, there are no periodic boundary conditions in the directions normal to the walls, which are located at $z=\pm L_z/2$. The simulations in this section are organized to investigate under what conditions the results presented in Fig. 1, in which smooth steel balls were used, can be reproduced. Note that it is likely that the granular assembly in Fig. 1 was highly cooled, resulting in the formation of an ordered crystal. As a result, the granular assembly had undergone a structural arrest, where self-diffusivity of the grains becomes zero. In this light, the particle diffusive motion will be monitored to distinguish a disordered state from an ordered system.

The first case is the bounded shear flow of a moderately dense system of about 10 000 smooth particles. The value of the solid fraction including the wall particles is close to 0.2, with the solid fraction of the wall particles slightly higher than that in the bulk. The particles with smooth surfaces, having a coefficient of restitution of $e_0=0.93$ and surface friction of $\mu=0$, are sheared at the apparent rate of 2 s^{-1} between walls separated by a distance $L_z \approx 30\sigma$. Here, the values of the particle surface parameters e and μ, for collisions between interior particles and wall particles are taken to be the same as those for collisions between interior particles. To ascertain that the period of the run was long enough for the system to come to a steady state, the normal stress at the upper wall was recorded. The time series for this quantity in a dimensionless form, $P^*=P/\rho_p\sigma^2\dot{\varepsilon}^2$, is illustrated in Fig. 10(a). Here, ρ_p is the material density. The eqiulibration period, which is the period during which all memory of the initial configuration is lost and the system comes to a steady state, was found to be $t^* \approx 20$. Ordering was not found to occur for this case, which implies that a strong particle diffusive motion would be expected in the direction of the velocity gradient. Given the presence of strong mixing in the system of smooth particles, an obvious question is how would the diffusive motion of the grains differ for the cases presented in Figs. 10(b) and 4(a). Note that the solid fraction of the bounded flow in Fig. 10(b) is the same as that of the unbounded flow of Fig. 4(a). To address this question, the diffusive motion of grains in a bounded shear flow at moderately high solid fractions is analyzed in the following section.

1. Lateral diffusive motion in a moderately dense bounded flow of smooth grains

The local descriptions for the velocity fields $\mathbf{V}(z)^* = [V(z)/V_{x0}]\mathbf{e}_x$ at $t^* \approx 30$, as illustrated in the inset of Fig. 10(a), are obtained in the same way as described in the preceding section. It is interesting to note that large slip veloci-

ties exist at the walls. Since the rate of temperature generation is controlled by shear work, these slips result in a large translational temperature near the wall, as shown in Fig. 10(c). The energy is transferred by means of thermal diffusion to the colder central region, in which the rate of energy generation is lower due to the moderate velocity gradient. Thermal diffusion is caused by the relative motion of the particles due to the presence of a translational temperature gradient. The drift induced by the temperature gradient, in a dimensionless form, may be characterized in terms of the thermal diffusion coefficient [26] D_T, which may be given as

$$\rho u_z^* = -\rho D_T^* \frac{\partial \ln T^*}{\partial z^*}. \tag{21}$$

In the above, ρ is the particle number density, $u_z^* = u_z/\sigma\dot{\varepsilon}$ represents the dimensionless diffusion velocity in the direction of velocity gradient, $z^* = z/\sigma$ is the dimensionless distance, $\dot{\varepsilon}$ is the apparent shear rate, and the dimensionless thermal diffusion is defined as $D_T^* = D_T/\sigma^2\dot{\varepsilon}$. In addition, if not all of the particles in the system are sheared uniformly as may occur in systems such as in [21] [also see Fig. 12(d)], then particles could migrate from the high-shear region at the wall to the low-shear region in the center. The drift induced by stress may be given as

$$\rho u_z^* = -B^* \frac{\partial \rho\, U^*(z)}{\partial z^*}, \tag{22}$$

where $B^* = B\dot{\varepsilon}$ is the dimensionless particle mobility and $U^*(z) = U(z)/(\sigma\dot{\varepsilon})^2$ represents a dimensionless potential. Approximate expressions for the particle mobility B and the potential U for a moderately dense system comprised of smooth particles are given in Appendix.

The above-mentioned drifts induce a particle number density gradient in the system, which results in a flux of the particles from the central region towards the wall. This flux caused by Fickian diffusion may be given as follows:

$$\rho u_z^* = -D_z^* \frac{\partial \rho}{\partial z^*}. \tag{23}$$

The net flux, with respect to the center of mass reference frame, is given by the sum of the fluxes (21)–(23):

$$\rho u_z^* = -\left(\rho D_T^* \frac{\partial \ln T^*}{\partial z^*} + B^* \frac{\partial \rho U^*(z)}{\partial z^*} + D_z^* \frac{\partial \rho}{\partial z^*} \right). \tag{24}$$

Substitution of this expression for the flux into the equation of continuity [52] yields the following result:

$$\frac{\partial \rho}{\partial t^*} = V^*(z)\frac{\partial \rho}{\partial x^*} - \frac{\partial}{\partial z^*}\left[\rho D_T^* \frac{\partial \ln T^*}{\partial z^*} + B^* \frac{\partial \rho\, U^*(z)}{\partial z^*} + D_z^* \frac{\partial \rho}{\partial z^*} \right], \tag{25}$$

where $x^* = 2x/L_z$ represents the dimensionless distance in the direction of mean flow.

Equation (25) provides a convenient picture for the particle diffusive motion in the lateral direction, for which the profiles of temperature and solid fraction are shown in Fig. 10. Since no simple solution exists for Eq. (25), it was suggested in [21] that a simplified form of Eq. (25), namely,

$$\frac{\partial \rho}{\partial t^*} = -D_z^* \frac{\partial^2 \rho}{\partial z^{*2}}, \tag{26}$$

might be of use in predicting the particle diffusive motion far from the walls in the fully developed part of their channel. Equation (26) addresses the local aggregation and redispersion of particles in the above-mentioned regions, which create local density fluctuations. Assuming that these fluctuations dissipate according to Fick's law, an expression may be obtained for the diffusion coefficient, namely, Eq. (19), which should be applied to the time regions where the mean-square displacement varies linearly with t^*

2. Particle diffusive motion and transition to order in dense bounded flows

The validity of Eq. (19) is questionable for a dense system whose local description for the velocity field, solid fraction, and temperature are given in Fig. 11, where the coefficient of restitution is $e_0 = 0.84$. However, in the absence of a more reliable theory for the treatment of particle diffusive motion in dense granular flows, Eq. (19) is used to estimate D_z^* for the tagged particles initially located at $-0.1 \leqslant z \leqslant 0.1$ in the central region, where the gradients may not be present. During the period of sampling of $\tau^* \approx 3$, no tagged particles were found to enter the wall region, in which neither the effects of gradients can be neglected nor the use of linear laws such as those used to obtain Eq. (26) is justified. Figure 11(f) illustrates the mean-square displacement in the z direction for the tagged particles, $\langle \Delta z^{*2} \rangle$, as a function of τ^*. At long times, $\langle \Delta z^{*2} \rangle$ appears to behave linearly in τ^* with $D_z^* \approx 0.054$, which is very close to the values of the dimensionless diffusivity measured in the experiments of Bridgwater [18]. It is worth mentioning that the calculation is based on the local value of shear rate, namely, 1.5 s^{-1}. The solid fraction and dimensionless temperature in the central region are found to be 0.58 and 1.38, respectively. The high granular temperature in the central region, which resulted in a high value for D_z^*, namely, 0.054, could also play a role in the stability of the flow. This observation also highlights the significant role of T^* in the particle diffusive motion in the lateral direction.

To focus on finding the dominant parameters in the stability analysis for the bounded flow, in the above-mentioned simulation of smooth particles using the modified hard-sphere model, the solid fraction is increased to a value of 0.59 and the apparent shear rate is decreased to 2 s^{-1} so that the local shear rate is nearly the same as that of the previous case. Although this solid fraction is beyond the recommended range of applicability for the hard-sphere model, the simulation results could nonetheless provide a rudimentary

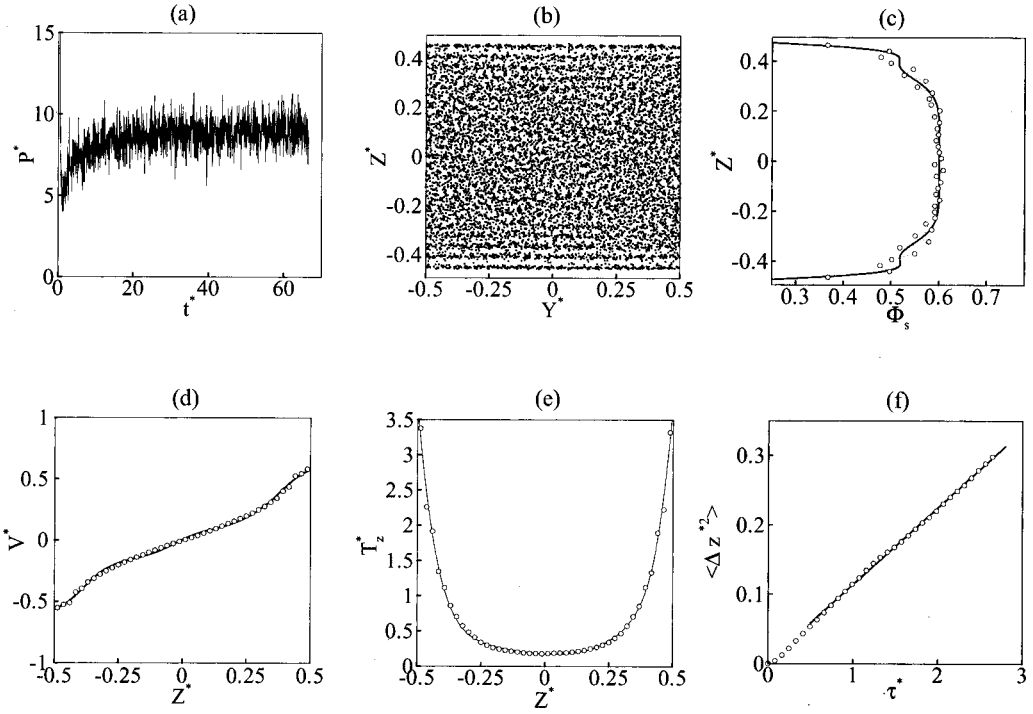

FIG. 11. (a) Dimensionless normal stress P^* exerted on the upper wall versus dimensionless time t^* for smooth particles at $\Phi_s \approx 0.565$ and the apparent shear rate of $\dot{\varepsilon} = 4\ \mathrm{s}^{-1}$, for $e_0 = 0.84$ and $\sigma^* \approx 0.048$. (b) Projection of interior particle positions onto the dimensionless yz plane for the sample taken at $t^* \approx 60$. (c) Variations of the local solid fraction of the sample shown in (b) with the dimensionless distance in the z direction. The dotted line corresponds to the solid fraction obtained using 42 bins. (d) Variations of the local dimensionless axial velocity $V(Z)^* = V(Z)/V_{0x}$ with Z^*. (e) Variations of T_z^* with Z^* for the apparent shear $\dot{\varepsilon} = 4\ \mathrm{s}^{-1}$. The solid lines in (c)–(e) are fits. (f) Variations of $\langle \Delta z^{*2} \rangle$ with the dimensionless delay time τ^* for the tagged particles initially located at $-0.1 \leqslant Z^* \leqslant 0.1$. The solid lines represent linear fits.

insight into ordering in dense granular systems. As seen in Fig. 12(a), the period of equilibration is long. The projection of the position of the interior particles onto the yz plane of a sample taken at $t^* \approx 100$ is illustrated in Fig. 12(b). As shown in this figure, the system had become ordered with the crystallized regions visible at $(-0.3,0) \times (-0.1,0.2)$ and $(0,0.3) \times (0.21,0)$. Figure 12(c) plots the variations of solid fractions in the direction of the velocity gradient. Contrary to what is observed in Fig. 11(c), this profile exhibits spikes in the central region, indicating the presence of layers of ordered particles in the system. Perhaps the most noticeable difference between the present case and the previous case can be found by comparing the steady-state values of the dimensionless normal stress at the walls, as shown in Figs. 11(a) and 12(a). It is surprising that the dimensionless normal stresses at higher solid fractions tended to be lower than those generated at lower solid fractions. The difference in stresses could be due to the smaller wall slip velocities, as illustrated in Fig. 12(d), which lead to the corresponding smaller rates of energy production. At high solid fractions, for particles in a layer adjacent to the wall, an enhancement in the particle-wall collision rates may be observed. The movement of a tagged particle away from the wall after a collision is limited due to the presence of a dense layer of moving particles in the neighboring layer below the particle. Upon colliding with a neighboring moving particle, a tagged particle is likely to travel back towards the wall particles. In this case, due to the enhancement in the rate of particle-wall collisions and also the limited displacement in the vertical direction, the particles are moved along horizontally with a velocity more correlated to that of the wall particles, which results in a smaller wall slip velocity. This observation suggests that the causes of smaller wall slip velocity at high solid fractions may be understood in terms of the relationship between the particle-wall and particle-particle collision rates.

As shown in Fig. 12(e), the lower production rates at the walls result in local temperatures that are below the melting temperature for this system, which leads to a transition to order. The results obtained suggest that rapid shear flows of smooth particles, at a very high solid fraction, become unstable with respect to a density wave in the direction of the velocity gradient. The phase transition as discussed above occurs when variations of the density and velocity fields are comparable to a particle diameter. In order to predict this behavior a theory should be devised which captures the critical wave number regime at intermediate wave numbers where the static structure factor $S(k_z)$ has its maximum, as shown in Fig. 13. This figure illustrates the static structure factor of a sample illustrated in Fig. 12(b) taken after $t^* \approx 100$. The static structure factor $S(k_z)$ was obtained from the initial value of the intermediate-scattering function, defined as [53]

$$F(k,t) = \langle Q(k,0) Q(-k,t) \rangle, \tag{27}$$

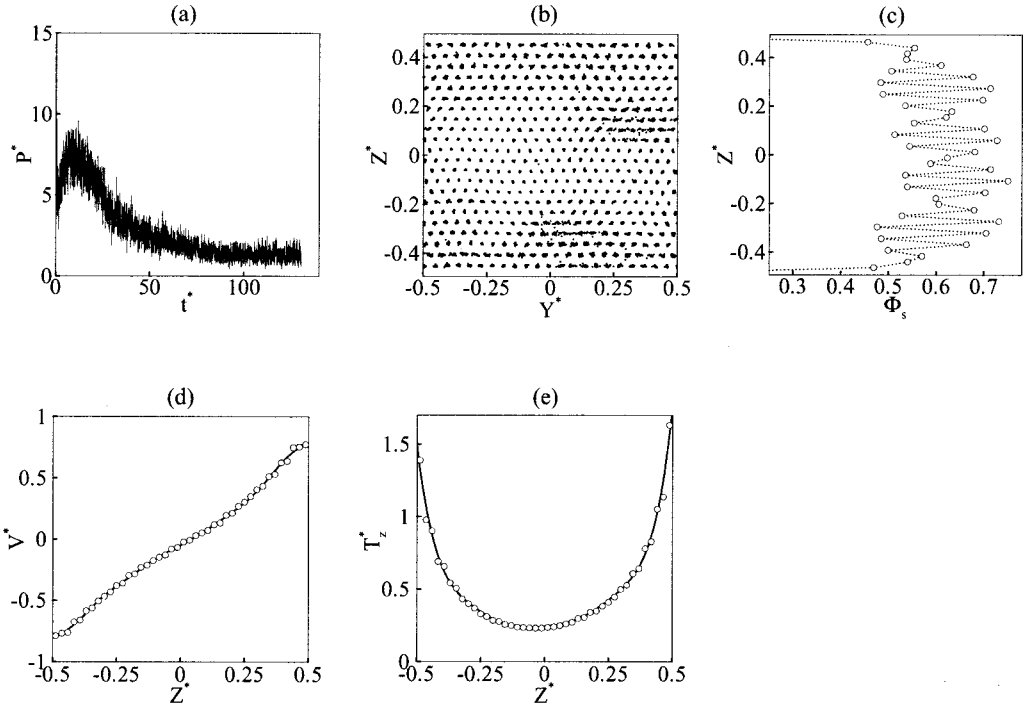

FIG. 12. (a) Dimensionless normal stress P^* exerted on the upper wall versus dimensionless time t^* for smooth particles at $\Phi_s \approx 0.59$ and the apparent shear rate of $\dot{\varepsilon} = 2\ s^{-1}$, for $e_0 = 0.84$ and $\sigma^* \approx 0.048$. (b) Projection of interior particle positions onto the dimensionless *yz* plane for the sample taken at $t^* \approx 100$. (c) Variations of the local solid fraction of the sample shown in (b) with Z^*. The dotted line corresponds to the solid fraction obtained using 42 bins. (d) Variations of the local dimensionless axial velocity $V(Z)^*$ with Z^*. (e) Variations of the local dimensionless translational temperature in the direction of velocity gradient T_z^* with Z^* for the apparent shear $\dot{\varepsilon} = 2\ s^{-1}$. The solid lines in (d), (e) are fits.

where $Q(k,t) = N^{1/2} \Sigma_{j=1}^{N} \exp[i\mathbf{k} \cdot \mathbf{r}_j(t)]$. Here, the attention is confined to **k** vectors in the *z* direction. The smallest wave number k_z that can be studied is $2\pi/L_z$. The dimensionless variable $k_z\sigma$ is used to express the structural correlation shown in Fig. 13, which provides a useful guide to structural effects on fluctuations. As seen in Fig. 13, the height of the first peak reaches a value of order *N*. This indicates the presence of a near-perfect layering into planes with well-defined layer spacing as seen in Fig. 12(b). The region of wave numbers where structural effects are expected to be strongest is near the first peak. It is interesting to observe that the second peak in $S(k_y)$, as illustrated in the inset of Fig. 13, becomes longer than the first peak. This observation may suggest the presence of regions of cuboctahedral symmetry in the computational box. Comparing the present results with Fig. 1, the hard-sphere model appears to be capturing qualitatively the flow behavior for a wide range of flow conditions.

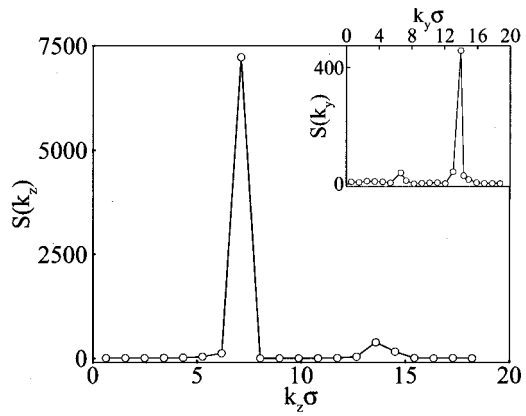

FIG. 13. Static structure factor $S(k_z)$ of a sample whose projection of interior particle positions onto the dimensionless *yz* plane is shown in Fig. 12(b). Inset: Static structure factor $S(k_y)$ of the same sample.

In order to show that the ordering transition persists and is not merely an artifact of the cubic computational box, the gap between the walls is reduced by approximately half. The initial configuration of interior particles projected onto the *yz* plane is shown in Fig. 14(a). To keep the solid fraction the same as the previous simulation, namely, 0.59, the number of interior and wall particles was reduced to 4296 and 400, respectively, with $L_z \approx 10\sigma$. The results for this run indicate a transition to order, evidence of which is shown in Fig. 14(b), which represents the configuration of interior particles projected onto the *yz* plane. Using the smooth particles, the stick-slip dynamics is observed in the time series of dimensionless normal stress, as shown in Fig. 14(d). This result is consistent with the recent findings by Miller, O'Hern, and Behringer [4], who have found that the stick-slip motion may vanish upon increasing the separation between the walls [54].

A similar behavior can be observed by comparing the time series of dimensionless normal stresses obtained at the same solid fraction, but with different separations between

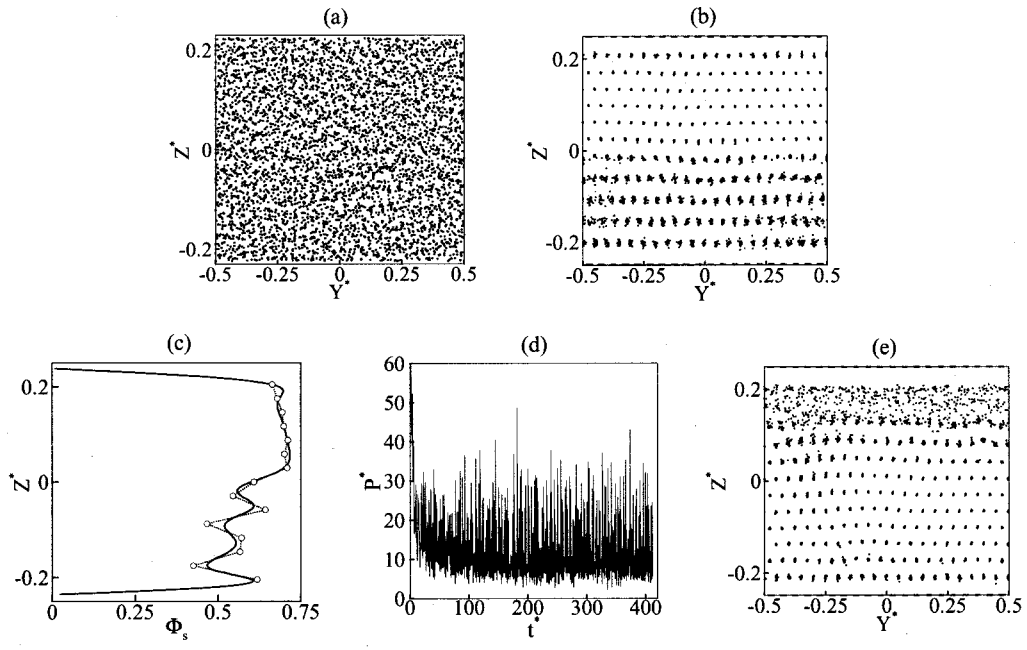

FIG. 14. (a) Projection of the positions of the interior particles onto the *yz* plane at the onset of shear. (b) Projection of the positions of the particles onto the *yz* plane at the steady-state condition for rough particles at $\Phi_s \approx 0.59$ and the apparent shear rate of $\dot{\varepsilon} = 4\ \mathrm{s}^{-1}$, for $e_0 = 0.84$ and $\sigma^* \approx 0.1$. (c) Variation of the local solid fraction of the sample shown in (b) as a function of Z^*. The dashed line corresponds to the solid fraction obtained using 17 bins. The solid line is a fit. (d) Dimensionless normal stress P^* exerted on the upper wall versus dimensionless time t^* at $\Phi_s \approx 0.59$ and the apparent shear rate of $\dot{\varepsilon} = 4\ \mathrm{s}^{-1}$ for $e_0 = 0.84$ and $\sigma^* \approx 0.1$. (e) Projection of the positions of the particles onto the *yz* plane for smooth particles at $\Phi_s \approx 0.59$ and the apparent shear rate of $\dot{\varepsilon} = 4\ \mathrm{s}^{-1}$, for $e_0 = 0.84$, $\sigma^* \approx 0.1$, and $\sigma\dot{\varepsilon}^2/g \approx 0.5$.

the walls, as shown in Figs. 12(a) and 14(d). Stick-slip motion has also been observed in studies of boundary lubrication [55]. In the present system stick-slip motion may be associated with the phase transition between ordered static and disordered kinetic states of the thin layer of particles separating the moving wall from the crystallized region located at $(-0.5,0.5)\times(0.05,0.18)$.

The mean dimensionless normal stress is about one order of magnitude greater in the present simulation than in the previous simulation with the same solid fraction but with different wall separation. The decreased wall separation most likely resulted in a different instability behavior, which caused the system to undergo a transition to a mixture of crystalline and noncrystalline two-phase flow with a nearly planar interface normal to the direction of the velocity gradient. Clearly, an explanation of this phenomenon requires a theoretical stability analysis, where variations of the density and velocity fields on the length scale of a particle diameter play a key role in the instability scenario. It is worth mentioning that the profile of the local solid fraction, as illustrated in Fig. 14(c), appears to be very similar to that for the experiments of [29], in which partial shearing occurred. However, in their system the formation of a nonshearable section adjacent to the bottom wall appears to be caused by gravity. In the presence of gravity, as can be seen in Fig. 14(e), the nonshearable section, whose density is higher than that of the surrounding fluid, has migrated downward. In order to take into account the effect of gravity, the collision times were calculated using the quartic equation (9) with $\mathbf{a}_i$, which represents the acceleration vector of the interior particles, set to $-2\sigma\dot{\varepsilon}^2\mathbf{e}_z$ m/s^2 directed in the negative z direction. The accelerations of the wall particles, $\mathbf{a}_w$, are assumed to be zero.

The absence of a disordered phase in the simulations at the high solid fraction of 0.59 suggests that the strong mixing reported in [21] is unlikely to be predicted for a system at this solid fraction. For this reason, the mean bulk solid fraction in [21] should be close to 0.565. Recall that at this solid fraction the simulation of shear flow of smooth particles with a wall separation of $L_z \approx 21\sigma$ resulted in a disordered phase in the central region with $D_z^* \approx 0.054$.

At this stage it would be useful to investigate the effect of wall separation distance on the flow stability. At the solid fraction of 0.565, the apparent shear of 4 s^{-1}, the wall separation of $L_z \approx 10\sigma$, and the surface parameters $e_0 = 0.84$, $\mu = 0$, the time series for the dimensionless normal stress is shown in the inset of Fig. 15(a). The mean value of the dimensionless normal stress in the interval of $150 < t^* < 350$ is found to be 15.5, which suggests that T_z^*, whose profile is illustrated in Fig. 15(a), is large enough to induce mixing. As seen from the inset of Fig. 15(b), the local shear rate in the central region is nearly constant, with a value very close to the apparent shear of 4 s^{-1}. Using Eq. (19) to estimate D_z^* for the tagged particles initially located at $-0.1 \leqslant Z^* \leqslant 0.1$, where the effects of gradients may be unimportant, results in a value of $D_z^* \approx 0.015$. According to the projection of the position of the interior particles onto the *yz* plane of a sample taken at $t^* \approx 150$, as shown in Fig. 15(d), some order in the central region can be observed, which

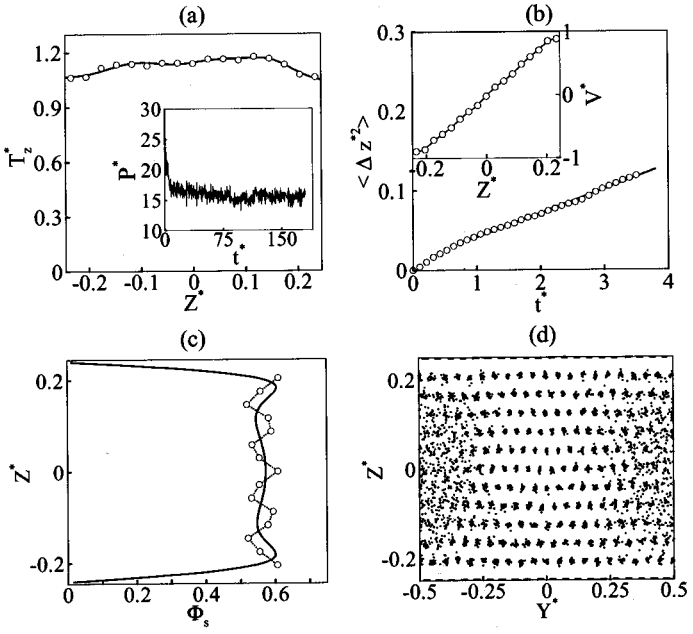

FIG. 15. (a) Variation T_z^* with Z^* for the apparent shear $\dot{\varepsilon}=4\ \mathrm{s}^{-1}$. The solid line is a fit. Inset: Dimensionless normal stress P^* exerted on the upper wall versus dimensionless time t^* for smooth particles at $\Phi_s \approx 0.565$ and the apparent shear rate of $\dot{\varepsilon}=4\ \mathrm{s}^{-1}$ for $e_0=0.84$ and $\sigma^* \approx 0.1$. (b) Variations of $\langle \Delta z^{*2} \rangle$ with the dimensionless delay time τ^* for the tagged particles initially located at $-0.1 \leqslant Z \leqslant 0.1$. The solid lines represent linear fits. Inset: Variations of $V(z)^*$ as a function of Z^*. The dashed line is a linear fit whose slope is very close to that of the apparent shear. The dotted line is a nonlinear fit. (c) Variation of the local solid fraction of the sample shown in (d) as a function Z^*. The dashed line corresponds to the solid fraction obtained using 17 bins. The solid line is a nonlinear fit. (d) The projection of the positions of the particles onto the dimensionless *yz* plane for a sample taken at $t^* \approx 150$.

explains the difference between the estimated values of D_z^* in the present case and the previous case. Again, this observation suggests that the separation between the walls plays a key role in the stability of the flow.

3. Bounded shear flow of rough particles

In the preceding section, simulations with frictionless, inelastic grains at a shear rate of 4 s^{-1} revealed that an initial configuration with random distributions of positions and velocities of particles may finally evolve to a state where an ordered solid phase is formed in a large part of the computational box as illustrated in Fig. 14(b). Thus, this configuration was selected as a new initial configuration for a series of simulations, to investigate the effect of phenomenological parameters on the vanishing of the ordered solid phase. It should be noted that the creation of the solid phase is independent of the initial random state, but depends mainly on the wall separation distance and the mean solid fraction. The view of the initial configuration of particles projected onto the *yz* plane as well as the variation of the local solid fraction in the direction of the velocity gradient are illustrated in Figs. 14(b) and 14(c), respectively. Computations were performed to explore the importance of the particle roughness on the vanishing of the ordered structure present in the initial configuration. Two different sets of values were used for the surface parameters e and μ, for steel pucks and glass beads, as introduced in the preceding section.

One signature of order in the system is the observed stick-slip motion in the normal stress signal, as discussed in the preceding section. Hence, the absence of stick-slip dynamics in the normal stress signal could serve as a criterion of the melting. Using the suggested values for surface parameters $e_0=0.93$, $\mu=0.123$, as illustrated in Fig. 16(a), the melting of granular crystals occurred after $t^* \approx 170$. The inset of Fig. 16(a) plots the probability densities for the dimensionless normal stress for both cases after the systems have reached a steady state. The observed shear-induced melting in the friction-dominated system may be interpreted considering the significance of rotational diffusion, which in a monodisperse system is a measure of the rate of change of the direction of bonds joining a particle with its nearest neighbors. In the aforementioned system the conversion of rotational energy to translational energy enhances the translational diffusion, which reduces the bond orientational order. This interesting combined translational-rotational diffusion process may warrant further investigation. More evidence supporting

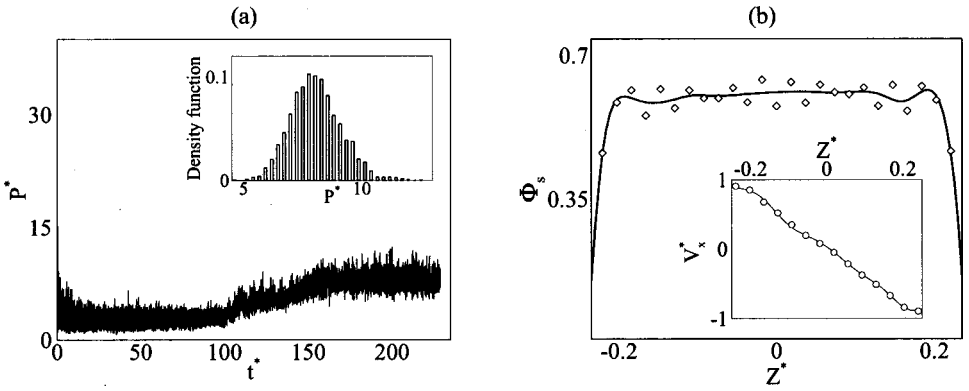

FIG. 16. (a) Dimensionless normal stress P^* as a function of t^*. Inset: The probability density function of the dimensionless normal stress at $t^* > 170$. (b) Variations of the solids fraction of a sample taken at $t^* \approx 170$ with Z^*. Inset: Variations of the corresponding V_x^* with Z^* at shear rate $\dot{\varepsilon}=4\ \mathrm{s}^{-1}$.

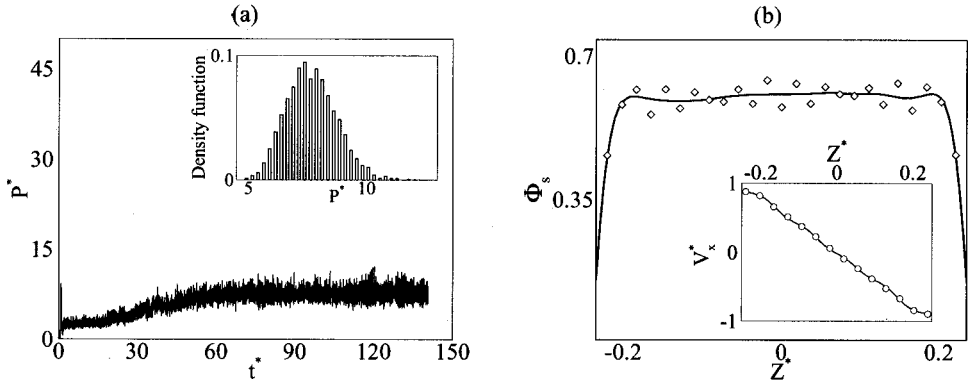

FIG. 17. (a) Variations of P^* with t^*. Inset: Probability density function of the dimensionless normal stress at $t^*>70$. (b) Variations of the solid fraction of a sample taken at $t^*\approx 70$ with Z^*. Inset: Variations of the corresponding V_x^* with Z^* at shear rate of $\dot{\varepsilon}=40\ s^{-1}$. The surface parameters are $e_0=0.93$, $\mu=0.123$, and $\beta_0=0.4$.

the aforementioned hypothesis is found considering the shorter melting time at an apparent shear rate of 40 s^{-1}, as shown in Fig. 17(a), compared to that illustrated in Fig. 16(a). For the same solid fraction and dissipation parameters, the rate of melting increases at the higher shear rate, due to higher rotational energy production. The slip velocity at the walls also increases, as shown in the insets of Figs. 16(b) and 17(b).

It can be argued that the order-disorder transition cannot be determined reliably by monitoring only the normal stress at the wall, which represents a macroscopic quantity of the system that may not convey the precise information of the local structure in the central region of the system. The vanishing of the ordered phase may be more reliably monitored by considering the time variations of the invariant quantity Q_6, which characterizes the average bond orientations in a system of particles. Initially, the value of Q_6 in the ordered phase [namely, $0.01\leqslant Z^*\leqslant 0.2$ in Fig. 14(b)] was found to be 0.5712, which is very close to the value of Q_6 for a system with cuboctahedral symmetry, namely, 0.574. It was observed that the values of Q_6 decrease sharply for the particle roughness parameters, such as those for glass beads or steel pucks, approaching steady-state values of Q_6 of 0.422 and 0.414, respectively, at the shear rate of 4 s^{-1}. These values for Q_6 imply that the frictional impulse changes the flow dynamics between the particles, resulting in a more rapid rate of vanishing of the ordered solid phase for the glass beads than for the steel pucks.

By comparing these results with those of real systems, such as the results shown in Fig. 1 in [4], it appears that neither the simulation performed using the particle surface properties of glass beads nor that with the particle surface properties of steel pucks fully reproduces the characteristics of real granular systems. In fact, the Gaussian form for the obtained probability distribution, as shown in the insets of Figs. 16(a) and 17(a), will give an entirely incorrect picture of the large-scale fluctuations observed in the experiments. Note that the instantaneous local values of the normal wall stresses have been found experimentally to be far larger than the mean, possibly as much as an order of magnitude [4], which indicates that the occurrence of these events are much more frequent than what would be predicted with the Gaussian form. It turns out that the major features observed in the experiments [4], as reported in their Fig. 1, such as the existence of instantaneous forces much larger the mean, can be reproduced using a system whose dynamics are collision dominated.

The plot of the probability density for the dimensionless normal stress signals of Fig. 14(d), as shown in Fig. 18, suggests that the occurrence of the large forces in the system in which the dynamics are collision dominated is much more likely with the exponential form than with the Gaussian form. These considerations imply that in the absence of gravity, bounded dense granular flows form ordered structures, provided the dynamics are collision dominated. Considering that the probability distributions of force in stationary bead packs can be described by an exponential function [56], the difference between the signals of the collision-dominated system and the friction-dominated system could well be attributed entirely to the existence of a solid region as shown in Fig. 14(b). More evidence supporting the aforementioned conjecture can be found by considering the dimensionless normal stress signals in the quasifluid phase adjacent to the bottom wall with the probability distributions of the Gaussian form. Note that the aforementioned quasifluid phase is a phase having some correlations in the orientations of particle clusters but is incapable of withstanding shear.

It appears that a hard-sphere model captures the essential physics for describing flow dynamics for a wide range of flow even at high solid fractions. However, an important difference exists between the sheared granular assembly as described in Fig. 14 and the granular flows reported in Ref. [4]. The representative spectra for 2-mm glass beads as presented in Fig. 2 of [4] do not display any sign of the periodic nature

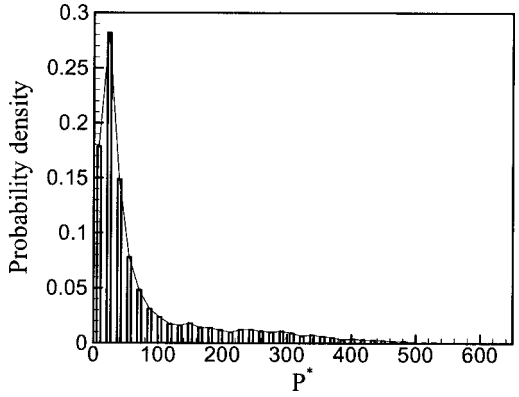

FIG. 18. Probability density function of the dimensionless normal stress P^* of Fig. 14(d).

in the corresponding signal. Therefore, the nature of the normal stress signal shown in Fig. 14(d) requires further investigation. To address this concern the signal is further analyzed using a space-scale map of wavelet transforms [57]. A simple understanding of the wavelet transform can be obtained by its analogy with the windowed Fourier transform in the similar time-frequency description of any given signal [57]. A wavelet function can be dilated or translated along the time axis t. These operations are characterized by two parameters, namely, scale, a, for dilation and center of wavelet, b, for translation. Any scale addresses a specific package of frequency contents in the wavelet. The stretched wavelets that correspond to large scales contain low frequencies, while the compressed wavelets corresponding to small scales have a high frequency content.

The wavelet transform of a function $f(t)$ using the wavelet ψ is simply defined as [57]

$$C(a,b)=\frac{1}{\sqrt{a}}\int f(t)\psi\left(\frac{t-b}{a}\right)dt. \tag{28}$$

Here a and b are real numbers that vary continuously in a continuous wavelet transform. A suitable type of wavelet for the present case is the Morlet wavelet, which has been previously used in the analysis of sound patterns [58]. By using such a complex-valued wavelet in the calculation of the wavelet coefficient modulus $C(a,b)$, the spurious oscillations [57] that could appear in visualizing the wavelet coefficient modulus may be eliminated. The mathematical expression of the complex-valued Morlet wavelet is given by [57]

$$\psi\left(\frac{t-b}{a}\right)=\frac{1}{\pi^{1/4}}\exp\left[-\frac{(t-b)^2}{2a^2}\right]\exp\left[i\frac{5(t-b)}{a}\right]. \tag{29}$$

As shown in Fig. 19(b), the modulus of wavelet coefficients of the signal in Fig. 14(c) shows strong analogy to that of a sawtooth sweep over the frequencies in Fig. 19(a). The sawtooth signal is in fact a sine wave that is subjected to a frequency decrease beyond a certain time. This frequency slip has been manifested as an increase of scale parameter in the corresponding map of the wavelet coefficient modulus, namely, larger scales represent lower frequencies. Thus the existence of higher frequencies can also be detected, shown as the horizontal green thin line at a lower scale in Fig. 19(b). Note that the scale axis of the wavelet coefficient modulus map in Fig. 19(a) is identical for the rest of maps in Fig. 19. The origin of the slight period changing shown in this figure might be associated with some dynamical instability in the sheared granular flow. These long lived frequencies have not been observed in the continuous wavelet transform of the signal in Fig. 16(a) corresponding to the frictional model, as shown in Fig. 19(c). Here, the wavelet transform of Gaussian white noise is shown in Fig. 19(d) for comparison. In light of the above, it may be concluded that the nature of the stick-slip motion in the annular Couette apparatus of [4] could be different from that found in the simulations. Apparently, the periodic nature of the signal as illustrated in Fig. 14(d) could be associated with the periodic shear-induced melting and reordering of the layer of particles adjacent to the wall.

B. Effects of gravity

As speculated by Thompson and Grest [2], the origin of stick-slip dynamics could be periodic dilatancy transitions and gravitational compactification. They found that at shear rates below a certain critical value, sheared granular flows are unstable to gravitational compactification. For such cases, only a portion of the material was sheared, while the rest of the material appeared to be in rigid-body motion below the shearing grains. This behavior gave rise to a shear-induced phase boundary between ordered and disordered states.

In order to reproduce the aforementioned behavior, simulations were carried out using a collision-dominated system in the presence of the gravitational acceleration, g m/s^2, with the initial configuration as shown in Fig. 14(b). In the simulations of this section, about 4300 glass beads were used, with a diameter of $\sigma=5$ mm and the density of $\rho=2500$ kg/m^3. The width, length, and height of the computational box were selected to be 10, 10, and 5 cm, respectively. The value of the dimensionless parameter $\sigma\dot{\varepsilon}^2/g$ is set to 0.5 and the coefficient of restitution is set to $e_0=0.84$. So that the simulations would as closely as possible resemble the experiments, the bottom wall was fixed and the top wall was set in motion with the velocity of $V_{0x}=22.5$ cm/s producing an apparent shear rate of $\dot{\varepsilon}=4.5\ \mathrm{s}^{-1}$. In the presence of gravity, after a very short time $t^*\approx 3$, the ordered solid phase, whose density is higher than that of the surrounding quasifluid phase, completely migrated downward, as shown in Fig. 14(e). After the settling time, a steady motion was observed where three layers of particles flowed over the ordered solid phase. These layers are shown in the inset of Fig. 20(a), which plots the local solid fraction as a function of Z. For these layers located in the region $Z>3.2$ cm, it is found that the value of $Q_6\sqrt{N_b}$ is 1.85. For this value, the phase that is formed over the ordered solid phase may be considered as a disordered phase. The profiles of the streamwise velocity component and granular temperature in the z direction for samples taken after $t^*>3$ are presented in Figs. 20(a) and 20(b), respectively. At the low shear rates, the constant-volume simulation with only the upper wall in motion results in a decay in the height of the fluid phase to the point where no shearing motion is possible. To prevent this from occurring, simulations were performed in which the upper wall was maintained at a constant load of $W\approx 3.0$ g N and was connected by a Hookian spring with a spring constant K to a driving motor and pushed with a constant velocity V_{0x} in the horizontal direction.

The simulations were continued using the surface parameters $e_0=0.84$, $\mu=0.41$. As shown in the preceding section of simple shear flow of rough particles, a chainlike cluster is likely to be formed in this system. After 10^8 collisions the generalized version of the nonlinear model (20) in which the effect of gravity is taken into account was utilized, which should be valid at any solid fraction. The preliminary results

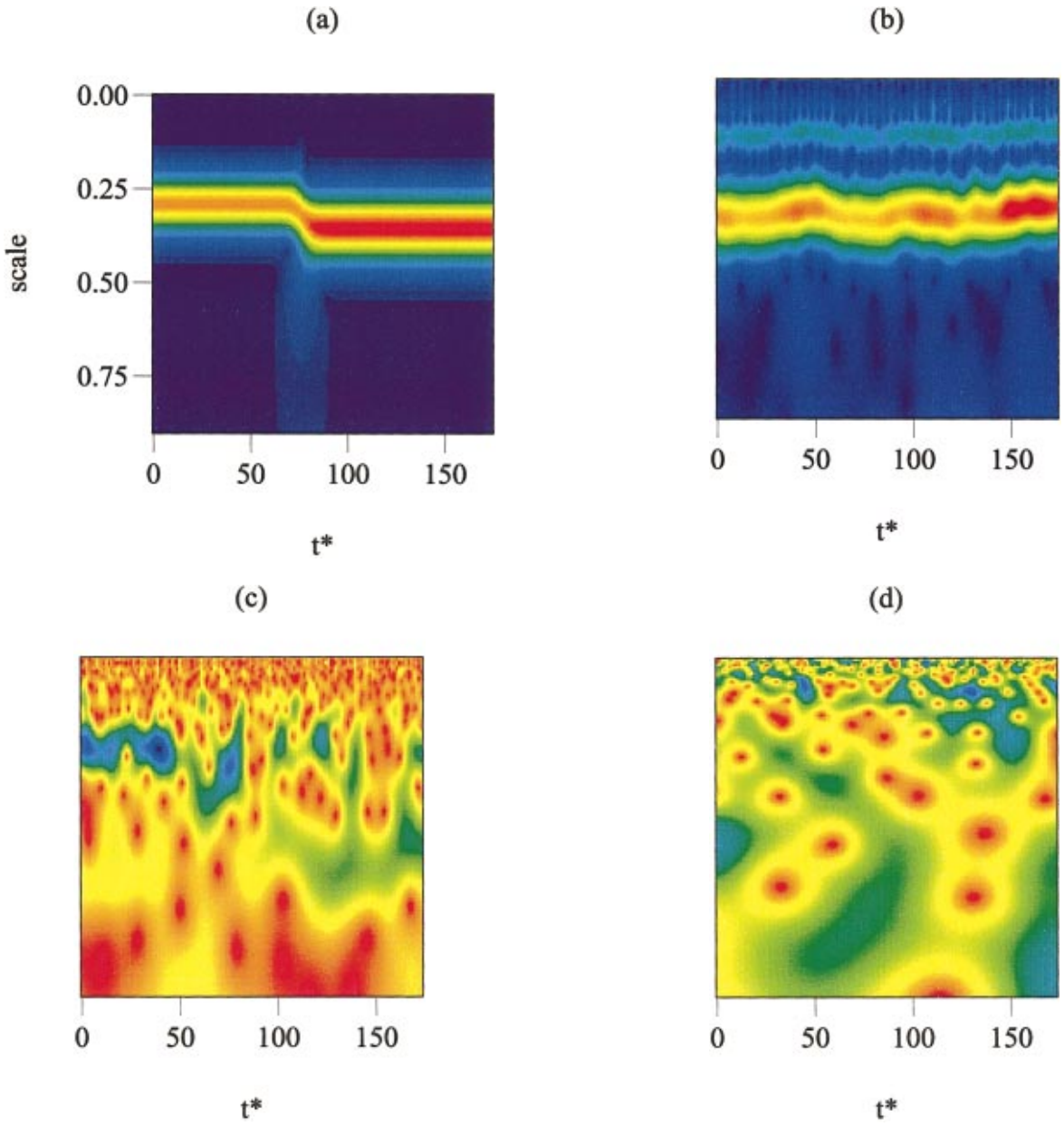

FIG. 19. (Color) Continuous wavelet transform. (a) Modulus of wavelet coefficients of a signal of period changing from 0.02 to 0.028 s. (b) Modulus of wavelet coefficients of time series of P^* at shear rate of $\dot{\varepsilon}=4\,\mathrm{s}^{-1}$ and the surface parameters of $e_0=0.93$ and $\mu=0$. (c) Modulus of wavelet coefficients of signal in Fig. 17(a) at $100<t^*<150$. (d) Modulus of wavelet coefficients of a Gaussian white noise.

of the dimensionless normal stress at the bottom wall in the steady-state condition are shown in Fig. 20(c). Apparently the signal is somewhat nonperiodic and the stick-slip dynamics can clearly be observed in the time series of dimensionless normal stress. However, longer simulations are required to obtain a more refined picture of the shearing motion of granular materials.

It is worth mentioning that the vertical motion of the upper wall in the opposite direction of gravity was observed. This motion, which could be due to the dilatancy of the granular material, might be linked to the formation of chains in the granular assembly. Convincing evidence may be found by considering the presence of an ordered solid phase that can withstand shear. The profiles of the local solid fraction and the local velocity, as illustrated in Fig. 20, should be very similar to those for the experiments of [29] in which the dilatancy of granular assembly was reported. It is quite likely that in their system the nonshearable section adjacent to the bottom was ordered. The signature of an ordered phase can also be seen in the background of the inset of Fig. 1 in [4]. Therefore, it may be speculated that during the compaction period, while the upper wall moves downward, the disordered layers of particles flowing over the ordered solid phase are compressed. At moderate shear rates, the thickness of the disordered layers is about three particle diameters. Therefore, a number of chainlike clusters could easily form in the com-

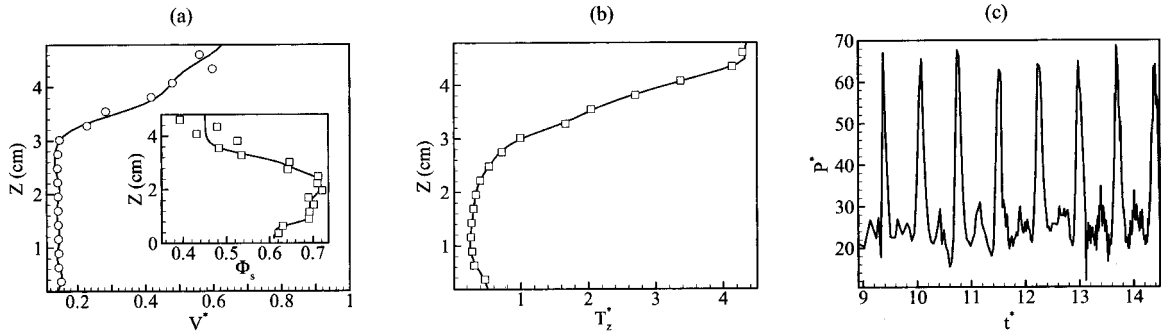

FIG. 20. (a) Dimensionless velocity V^* as a function of distance in the z direction for glass beads under gravitational compaction process. The top wall was set in motion horizontally with a velocity of $V_{0x}=22.5$ cm/s producing a shear rate of $\dot{\varepsilon}=4.5\ \mathrm{s}^{-1}$ with $\sigma\dot{\varepsilon}^2/g\approx 0.5$. The thickness of the nonsharable region is about 3.2 cm and the thickness of the disordered phase is 1.5 cm. Inset: Solid fraction as a function of distance in the z direction. (b) Dimensionless translational granular temperature T_z^* as a function of distance in the z direction. The solid lines are nonlinear fits. (c) Typical time series for the dimensionless stress P^* as a function of dimensionless time t^* obtained using the generalized version of the nonlinear model in which the effect of gravity is taken into account. The simulation parameters are same as used in (a).

pressed disordered layers between the upper wall and the ordered phase, resulting in the cessation of the shearing motion. In order to have continuous shearing, the granular assembly would then have to dilate. It is of great interest to find out whether chainlike clusters would form during the dilation period. To this end the processes of formation and disintegration of clusters were carefully monitored. It appears that some arches could also form during the dilation period at the moderate shear rates mentioned above. However, at high shear rates where the thickness of the disordered layers is quite large, a more smooth continuous shearing motion would be expected. These observations enhance the understanding of the complex processes involved in the experiments of Refs. [4,29]. The stick-slip phenomenon in granular flows is an interesting phenomenon that merits further investigation.

V. CONCLUSIONS

The shear-induced motion of granular assemblies comprised of a large number of viscoelastic, monosized, spherical particles in both unbounded and bounded systems was investigated using computer simulations. The solid fraction was varied from a low density system of 0.16 to a very high density system of 0.59. Two different models were used for predicting the flow dynamics of granular assemblies, namely, the modified hard-sphere model in which collisions between the grains are assumed to be instantaneous, and the more computationally intensive particle dynamics model in which the collisions have finite durations. A Hertzian-type model for the treatment of the viscoelastic behavior of the particles in contact was also introduced.

The modified hard-sphere model was shown to replicate reasonably well some of the results predicted by kinetic theory [25] at low and moderate solid fractions. Furthermore, this model was found to predict the basic features such as particle lateral diffusive motion in real sheared granular flows, even at a high value of the solid fraction of 0.56. However, it was found that it would be difficult to simulate complex phenomena, such as jamming in systems with constant volume, at values of the solid fraction larger than 0.58 using hard-sphere models. For these systems, the particle dynamic model was found to more closely predict the formation of clusters when nonlinear viscoelastic grain behavior was assumed, as opposed to previously proposed linear models [2,9,10]. An even more reasonable representation of cluster formation was found by including the effects of surface friction in the model. Comparing the simulation results with the results of experiments in which force fluctuations were measured [4], it was found that a nonlinear model for the viscoelastic frictional grains could predict the behavior of the chainlike clusters more precisely than a linear model. However, neither frictionless nor frictional particle models were capable of predicting observed particle ordering [6] in unbounded flows. It is likely that in the system in which the wall effects are not significant, the sheared granular assembly transforms to a glass state at solid fractions above 0.58.

Particle ordering was predicted using the modified hard-sphere model for simulations of frictionless granular systems in bounded shear flows even in the absence of gravity. It was also found that the local solid fraction and the wall separation distance govern the stability of the flow. Values were determined for the solid fraction and the wall separation distances at which a transition to order occurs. In these systems the presence of an exponential behavior of the probability distribution function was found in the normal stress signals exerted on the wall, consistent with experimentally observed force fluctuations [4]. Wavelet transform analysis was used to show the existence of a characteristic frequency in the normal stress signal, indicating the presence of stick-slip dynamics. For the range of shear rates studied, the simulation results for the rough model did not show the same stick-slip behavior due to the vanishing of the ordered solid region caused by the presence of strong frictional interactions. Recall that in [6] no order was observed using rough particles in the experiments.

The diffusive behavior of particles at moderately dense solid fractions in bounded flows was analyzed using a comprehensive model based on the revised Enskog theory of

granular fluids and on Grad's method of moments. Formal expressions were derived for the particle self-diffusion coefficient, particle thermal diffusion coefficient, and coefficient of mobility. Additional theoretical study is required to characterize further the particle diffusive motion in dense systems where cluster diffusion seems to be important.

Considering the ratio of the impact duration and the mean free time, the hard-sphere model was found to be appropriate for solids fractions below 0.56. Above this value, a particle dynamics model is recommended. However, it was shown that the hard-sphere model could provide a rough picture of the shearing flow of the granular assembly even at solid fractions above 0.56. It was shown that the rough picture provided by the hard-sphere model could be refined using the nonlinear particle dynamics model. For example, in order to consider the effect of gravitational compactification, a study was performed in which gravity was considered and the vertical motion of the upper wall was allowed. The modified hard-sphere model correctly predicted the formation of a disordered layer of particles over the ordered solid phase in a shearing motion of a granular assembly. The simulations were continued using a nonlinear particle dynamics model, which predicted the cluster formation more precisely. For these conditions chain formation was found to be quite likely in the disordered layers for frictional particles. The interesting stick-slip dynamics could be clearly observed in the normal stress signal for the bottom wall.

Fresh interpretations were given for the complex processes observed in experiments of Refs. [4,29]. Additional study is required to characterize further the flow dynamics of a granular assembly. Such a study should lead to the development of advanced theories capable of describing complex processes in granular flows, which are of real significance in facilitating the design of practical granular flow systems. To complement the simulation studies, additional experimental results should be obtained, for which vital information such as solid fractions and particle surface properties should be reported. The absence of such information limits the advances in the knowledge of the physics of granular flows that could be obtained through comparisons of experimental and numerical results.

ACKNOWLEDGMENTS

The authors would like to thank Dr. Goodarz Ahmadi for providing the results shown in Fig. 1. They are also grateful to Dr. Donald Gugan for helpful discussions. Computing time provided by the Finnish Center for High-Performance Computing and Networking is gratefully acknowledged. P.Z. acknowledges the support of the Finnish Academy, Grant No. 74846.

APPENDIX

Consider a granular material consisting of a binary mixture of differently colored smooth, spherical particles. For this system, light and dark colors are represented by subscripts l and d, respectively. The particles, which have the same masses m and radii σ but different number densities n^l and n^d, are sheared at a high shear rate. Due to the presence of gradients in the mean flow, random fluctuations in the local mean translational motion of the grains are generated. Since the particles in a rapid shear flow behave similar to molecules in a dense gas, methods from the kinetic theory of dense gases [59] might be used to describe the motion of particles in this system. For a nonequilibrium granular fluid, in the limit of two-body forces between the particles, the probability that at some instant of time t a particle of kind l will be at location $\mathbf{r}$ and have momentum $\mathbf{p}$ within the respective limits $d\mathbf{r}$ and $d\mathbf{p}$ may be governed by the following equation [52]:

$$\frac{\partial f^{l^{(1)}}}{\partial t}+\mathbf{c}^l\cdot\frac{\partial f^{l^{(1)}}}{\partial \mathbf{r}}+\mathbf{F}^l\cdot\frac{\partial f^{l^{(1)}}}{\partial \mathbf{c}}=-\int\int \mathbf{X}^{l,m}\cdot\frac{\partial f^{lm^{(2)}}}{\partial \mathbf{c}}d\mathbf{r}^m d\mathbf{p}^m. \tag{A1}$$

Here $\mathbf{c}^l$ is the instantaneous velocity of a particle of kind l, $\mathbf{X}^{lm}$ is the force on a particle of kind l due to all other particles, and $\mathbf{F}^l$ is the force per unit mass acting on a particle of kind l due to external fields.

Equation (A1) involves the pair distribution function $f^{lm^{(2)}}$, which is the probability that there is simultaneously a particle of kind l in the space element $(d\mathbf{r}^l d\mathbf{p}^l)$ about $(\mathbf{r}^l,\mathbf{p}^l)$ and another particle of kind m, which can be either light or dark, in the space element $(d\mathbf{r}^m d\mathbf{p}^m)$ about $(\mathbf{r}^m,\mathbf{p}^m)$. Thus, it is needed to find an expression for the pair distribution function in terms of single particle distribution functions. If the particle contacts can be regarded as nearly instantaneous collisions, the distribution functions do not change appreciably in a time interval comparable to the duration of a collision, the gradients of inhomogeneities are small, and the assumption of particle chaos remains valid, Eq. (A1) reduces to the generalized Boltzmann equation which governs the temporal change of the single particle distribution function of the particle of kind l. Since the particle diffusion processes involved in a granular fluid are of interest in the present study, the new variable $\mathbf{C}^l=\mathbf{c}^l-\mathbf{V}$, which is the particle peculiar velocity, is introduced in place of $\mathbf{c}^l$ into Eq. (A1). As a result, the following kinetic equation is obtained [59]:

$$\begin{aligned}\frac{df^{l^{(1)}}(\mathbf{r},\mathbf{C},t)}{dt}&=\left[-\mathbf{C}^l\cdot\frac{\partial}{\partial\mathbf{r}}+\left(\frac{\partial\mathbf{u}}{\partial\mathbf{r}}\right):\left(\mathbf{C}^l\frac{\partial}{\partial\mathbf{C}}\right)+\left(\frac{d\mathbf{u}}{dt}\cdot\frac{\partial}{\partial\mathbf{C}}-\mathbf{F}^l\frac{\partial}{\partial\mathbf{C}}\right)\right]\\&\times f^{l^{(1)}}(\mathbf{r},\mathbf{C},t)+\sum_{m=l}^{d}\int\int\sigma^2[g^{lm}(\mathbf{r},\mathbf{r}+\sigma\mathbf{k}|\{n^s\})\\&\times f^{l^{(1)}}(\mathbf{r},\mathbf{C}^l,t)f^{m^{(1)}}(\mathbf{r}+\sigma\mathbf{k},\mathbf{C}^m,t)\\&-g^{lm}(\mathbf{r},\mathbf{r}-\sigma\mathbf{k}|\{n^s\})f^{l^{(1)}}(\mathbf{r},\mathbf{C}^l,t)f^{m^{(1)}}(\mathbf{r}-\sigma\mathbf{k},\mathbf{C}^m,t)]\\&\times(\mathbf{c}^{lm}\cdot\mathbf{k})H(\mathbf{c}^{lm}\cdot\mathbf{k})d\mathbf{k}\,d\mathbf{c}^m,\end{aligned} \tag{A2}$$

Here $d/dt=\partial/\partial t+\mathbf{V}\cdot\partial/\partial\mathbf{r}$ is the substantial time derivative, $\{n^s\}=\{n^l,n^d\}$ are solid component densities, $\mathbf{V}=\Sigma_{m=l}^{d}m^m\mathbf{c}^m/\Sigma_{m=l}^{d}m^m$ is the mean mass velocity of the mixture, $\mathbf{c}^{lm}=\mathbf{c}^l-\mathbf{c}^m$ is the relative velocity of the two particles of kind l and kind m, $\mathbf{k}$ is the unit vector directed along the line from the center of the particle of kind m to the center of the particle of kind l at contact, and H is the Heaviside step function. Also, factors g^{lm} are introduced to take into account the difference in position of the colliding particles in binary collision dynamics, and the resulting increase in the frequency of collisions. Following van Beijeren and Ernst [60], g^{lm} are chosen to be the mixture radial distribution functions at contact, which are evaluated as nonlocal functionals of the density fields of the two components in the granular fluid mixture. Thus,

$$\begin{aligned}g^{lm}&(\mathbf{r},\mathbf{r}\pm\sigma\mathbf{k}|\{n_s(\mathbf{r})\})\\&=g_c^{lm}(\sigma|\{n_s(\mathbf{r})\})\\&\quad+\sum_{q=l}^{d}\int d\mathbf{r}^q H^{lmq}(\mathbf{r},\mathbf{r}\pm\sigma\mathbf{k},\mathbf{r}^q|\{n^s(\mathbf{r})\})(\mathbf{r}^q-\mathbf{r})\cdot\frac{\partial n^q}{\partial\mathbf{r}}\\&\quad+O(\nabla^2).\end{aligned}\tag{A3}$$

In the above equation, g_c^{lm} is the equilibrium value of the radial distribution function at contact for particles of kind l and m:

$$\begin{aligned}g_c^{lm}&(\sigma|\{n^s(\mathbf{r})\})\\&=1+\sum_{q=1}^{d}n^q(\mathbf{r})\int V^{lmp}(\mathbf{r},\mathbf{r}\pm\sigma\mathbf{k}|_{\mathbf{r}^q})d\mathbf{r}^q+\cdots.\end{aligned}\tag{A4}$$

Here, $H^{lmq}(\mathbf{r},\mathbf{r}\pm\sigma\mathbf{k},\mathbf{r}^q|\{n^s(r)\})=V^{lmq}(\mathbf{r},\mathbf{r}\pm\sigma\mathbf{k}|\mathbf{r}^q)+\Sigma_{q'=1}^{m}n^{q'}(\mathbf{r})\int V^{lmqq'}(\mathbf{r},\mathbf{r}\pm\sigma\mathbf{k}|\mathbf{r}^q\mathbf{r}^{q'})d\mathbf{r}^{q'}+\cdots$, which is symmetric under the interchange of superscript l and m. Also, $V(\mathbf{r},\mathbf{r}\pm\sigma\mathbf{k}|\mathbf{r}^q)$ and $V(\mathbf{r},\mathbf{r}\pm\sigma\mathbf{k}|\mathbf{r}^q\mathbf{r}^{q'})$ represent Husimi functions. As discussed earlier, the above approximation for the radial distribution function at contact is not quite appropriate for the present study of a sheared granular flow where a spatial preference for collisions is imposed by the velocity field. However, there is presently no better approximation available.

To derive the hydrodynamic equations of a granular fluid mixture, which are valid outside the time regime for which Eq. (A2) is exact. This equation is first multiplied by $m\psi^l$, where ψ^l is any property of the particles of kind l. The resulting equation is then integrated over the instantaneous velocity $\mathbf{c}_l$ to give the equation of change for the assembly of particles of kind l in terms of the mass-weighted mean values:

$$\begin{aligned}&\frac{d}{dt}(\rho_m^l\Phi^l\overline{\psi^l})+\rho_m^l\Phi^l\overline{\psi^l}\frac{\partial}{\partial\mathbf{r}}\cdot\mathbf{V}\\&\quad=\rho_m^l\Phi^l\frac{d\overline{\psi^l}}{dt}-\frac{\partial}{\partial\mathbf{r}}\cdot(\rho_m^l\Phi^l\overline{\mathbf{C}^l\psi^l})-\rho_m^l\Phi^l\frac{d\mathbf{V}}{dt}\cdot\frac{\overline{\partial\psi^l}}{\partial\mathbf{C}}\\&\quad\quad-\rho_m^l\Phi^l\left(\frac{\partial\mathbf{V}}{\partial\mathbf{r}}\right):\overline{\mathbf{C}^l\frac{\partial\psi^l}{\partial\mathbf{C}}}+\rho_m^l\Phi^l\overline{\mathbf{F}^l\cdot\frac{\partial\psi^l}{\partial\mathbf{C}}}\\&\quad\quad+\rho_m^l\Phi^l\overline{\mathbf{C}^l\cdot\frac{\partial\psi^l}{\partial\mathbf{r}}}+\sum_{m=1}^{d}\left\langle\chi^{lm}(\psi^l)-\frac{\partial}{\partial\mathbf{r}}\cdot\Theta^{lm}(\psi^l)\right.\\&\quad\quad-\frac{1}{2}\int\int\int m\sigma^3\left[\left(\mathbf{k}\frac{\partial(\psi^{l'}-\psi^l)}{\partial\mathbf{C}^l}\right):\left(\frac{\partial\mathbf{V}}{\partial\mathbf{r}}\right)\right]\\&\quad\quad\times(\mathbf{c}^{lp}\cdot\mathbf{k})H(\mathbf{c}^{lp}\cdot\mathbf{k})f^{m^{(1)}}(\mathbf{r},\mathbf{C}^m,t)f^{l^{(1)}}(\mathbf{r},\mathbf{C}^l,t)g_c^{lp}\\&\quad\quad\times\left\{1+\frac{\sigma}{2}\mathbf{k}\cdot\frac{\partial}{\partial\mathbf{r}}\left[\ln\frac{f^{m^{(1)}}(\mathbf{r},\mathbf{C}^m,t)}{f^{t^{(1)}}(\mathbf{r},\mathbf{C}^l,t)}\right]\right.\\&\quad\quad\left.\left.+\cdots\right\}d\mathbf{k}\,d\mathbf{c}^l d\mathbf{c}^m\right\rangle.\end{aligned}\tag{A5}$$

Here ρ_m^l and Φ^l are the material density and solid volume fraction of the particles of kind l. Expressions for the particle-particle collisional flux Θ^{lm} and the sourcelike term χ^{lm} are given as follows:

$$\begin{aligned}\Theta^{lm}(\psi)&=-\frac{1}{2}\int\int\int m(\psi^{l'}-\psi^l)\mathbf{k}\sigma^3(\mathbf{c}^{lm}\cdot\mathbf{k})H(\mathbf{c}^{lm}\cdot\mathbf{k})\\&\quad\times g_c^{lm}f^{m^{(1)}}(\mathbf{r},\mathbf{C}^m,t)f^{l^{(1)}}(\mathbf{r},\mathbf{C}^l,t)\\&\quad\times\left\{1+\frac{1}{2}\sigma\mathbf{k}\cdot\frac{\partial}{\partial\mathbf{r}}\left[\ln\frac{f^{m^{(1)}}(\mathbf{r},\mathbf{C}^m,t)}{f^{(l)^{(1)}}(\mathbf{r},\mathbf{C}^l,t)}\right]+\cdots\right\}\\&\quad\times d\mathbf{k}\,d\mathbf{c}^l d\mathbf{c}^m,\\\chi^{lm}(\psi)&=\frac{1}{2}\int\int\int m(\psi^{l'}+\psi^{m'}-\psi^l-\psi^m)\\&\quad\times\sigma^2(\mathbf{c}^{lm}\cdot\mathbf{k})H(\mathbf{c}^{lm}\cdot\mathbf{k})g_c^{lm}f^{m^{(1)}}(\mathbf{r},\mathbf{C}^m,t)f^{l^{(1)}}\\&\quad\times(\mathbf{r},\mathbf{C}^l,t)\\&\quad\times\left\{1+\frac{1}{2}\sigma\mathbf{k}\cdot\frac{\partial}{\partial\mathbf{r}}\left[\ln\frac{f^{m^{(1)}}(\mathbf{r},\mathbf{C}^m,t)}{f^{l^{(1)}}(\mathbf{r},\mathbf{C}^l,t)}\right]+\cdots\right\}\\&\quad\times d\mathbf{k}\,d\mathbf{c}^l d\mathbf{c}^m\quad\text{for } m=l,\\\chi^{lm}(\psi)&=\int\int\int m(\psi^{l'}-\psi^l)\sigma^2(\mathbf{c}^{lm}\cdot\mathbf{k})H(\mathbf{c}^{lm}\cdot\mathbf{k})g_c^{lm}\\&\quad\times f^{m^{(1)}}(\mathbf{r},\mathbf{C}^m,t)f^{l^{(1)}}(\mathbf{r},\mathbf{C}^l,t)\left\{1+\tfrac{1}{2}\sigma\mathbf{k}\cdot\frac{\partial}{\partial\mathbf{r}}\right.\\&\quad\times\left.\left[\ln\frac{f^{m^{(1)}}(\mathbf{r},\mathbf{C}^m,t)}{f^{l^{(1)}}(\mathbf{r},\mathbf{C}^l,t)}\right]+\cdots\right\}d\mathbf{k}\,d\mathbf{c}^l d\mathbf{c}^m\\&\quad\text{for } m\neq l.\end{aligned}\tag{A6}$$

The equations of conservation of mass, momentum, and energy for a granular assembly of kind l may be derived by taking ψ^l in Eq. (A5) to be 1, $\mathbf{C}^l$, and $\mathbf{C}^{l^2}$, respectively.

(i) Balance of mass

$$\frac{d\rho^l}{dt}+\rho^l\frac{\partial}{\partial\mathbf{r}}\cdot\mathbf{V}+\frac{\partial}{\partial\mathbf{r}}\cdot(\rho^l\mathbf{u}^l)=0, \tag{A7}$$

where $\rho^l=\rho_m^l\Phi^l$ is the apparent density and $\mathbf{u}^l$ is the diffusion velocity of particles of kind l.

(ii) Balance of linear momentum

$$\rho^l\frac{d\mathbf{V}^l}{dt}-\mathbf{V}^l\frac{\partial}{\partial\mathbf{r}}\cdot(\rho^l\mathbf{V}^l)=-\frac{\partial}{\partial\mathbf{r}}\cdot\mathbf{\Pi}^l+\rho^l\overline{\mathbf{F}^l}-\rho^l\frac{d\mathbf{V}}{dt}-\rho^l\frac{\partial\mathbf{V}}{\partial\mathbf{r}}\cdot\mathbf{V}^l+\sum_{m=1}^{d}\chi^{lm}(\mathbf{C}^l), \tag{A8}$$

where $\mathbf{V}^l$ and $\mathbf{\Pi}^l$ are the velocity vector and the macroscopic pressure tensor of particles of kind l, respectively.

(iii) Balance of kinetic energy (pseudothermal energy)

$$\frac{3}{2}\left\{n^l\frac{dT}{dt}-T\frac{\partial}{\partial\mathbf{r}}\cdot(n^l\overline{\mathbf{C}}^l)\right\}=-\frac{\partial}{\partial\mathbf{r}}\cdot\mathbf{q}^l-\gamma^l-\mathbf{\Pi}^l:\frac{\partial\mathbf{V}}{\partial\mathbf{r}}+\rho^l\overline{\mathbf{F}^l\cdot\mathbf{C}^l}-\rho^l\overline{\mathbf{C}}^l\cdot\frac{d\mathbf{V}}{dt}, \tag{A9}$$

where $T=1/3C^{l^2}$ is the mixture pseudothermal energy, $\mathbf{q}^l$ is the energy flux vector of particles of kind l, and γ^l is the rate of energy dissipation of particles of kind l per unit volume of the mixture due to the inelastic nature of the collisions. The effect of the thermal energy on the particle elasticity is not considered in the present treatment.

Assuming that the rapid shearing motion of a binary mixture of differently colored granular fluids can be adequately described by the consideration of the 13-moment approximation [61], expressions for the macroscopic pressure tensor $\mathbf{\Pi}^l$, energy flux vector $\mathbf{q}^l$, and sourcelike terms $\chi^{lm}(\mathbf{C}^l)$ and γ^l are given as follows [25]:

$$\mathbf{\Pi}^l=(\rho^lT\mathbf{I}+\rho^l\mathbf{a}^{\dagger l})+\sum_{m=1}^{d}(1+e_0)\rho^ln^m\sigma^3g_c^{lm}\left\{\frac{\pi}{3}T\mathbf{I}+\frac{\pi}{15}(\mathbf{a}^{\dagger l}+\mathbf{a}^{\dagger m})-\frac{4}{15}\sigma(nT)^{1/2}\left[\frac{\overset{\circ}{\overline{\overline{\partial\mathbf{V}}}}}{\partial\mathbf{r}}+\frac{5}{6}\left(\frac{\partial}{\partial\mathbf{r}}\cdot\mathbf{V}\right)\mathbf{I}\right]\right\}, \tag{A10}$$

$$\mathbf{q}^l=\tfrac{5}{2}\rho^l(T\mathbf{v}^l+\tfrac{1}{5}\mathbf{a}^l)+\sum_{m=l}^{d}\sigma^3g_c^{lm}(1+e_0)\Bigg\langle-\sigma(nT)^{1/2}\times\left\{\frac{m}{6}T(1-e_0)\left(n^m\frac{\partial n^l}{\partial\mathbf{r}}-n^l\frac{\partial n^m}{\partial\mathbf{r}}\right)+\tfrac{1}{3}n^m\rho^l\frac{\partial T}{\partial\mathbf{r}}\right\}+\pi n^m\rho^lT[\tfrac{1}{6}(\mathbf{u}^m+\mathbf{u}^l)+\tfrac{1}{4}(1-e_0)(\mathbf{u}^m-\mathbf{u}^l)]+\frac{\pi}{20}n^m\rho^l[(\mathbf{a}^m+\mathbf{a}^l)+\tfrac{1}{2}(1-e_0)(\mathbf{a}^m-\mathbf{a}^l)]\Bigg\rangle, \tag{A11}$$

$$\chi^{lm}(\mathbf{C})=\sigma^2(1+e_0)g_c^{lm}\rho^ln^m\left\{\frac{\pi}{3}\sigma\left[-T\frac{n^l}{n^m}\frac{\partial}{\partial\mathbf{r}}\left(\frac{n^m}{n^l}\right)\right]-\tfrac{4}{3}(nT)^{1/2}(\mathbf{u}^l-\mathbf{u}^m)+\tfrac{1}{15}\left(\frac{\pi}{T}\right)^{1/2}(\mathbf{a}^l-\mathbf{a}^m)\right\}, \tag{A12}$$

$$\gamma^l=\sum_{m=l}^{d}2\sigma^2(1-e_0^2)g_c^{lm}n^m\rho^lT\left[(\pi T)^{1/2}-\frac{\pi}{4}\sigma\frac{\partial}{\partial\mathbf{r}}\cdot\mathbf{u}\right]. \tag{A13}$$

In the above, $\mathbf{a}^{\dagger m}$ is the pressure deviator, $\mathbf{a}^m$ is the transport pseudothermal energy flux vector, e_0 is the coefficient of restitution, and $\overset{\circ}{\overline{\overline{\partial\mathbf{V}}}}/\partial\mathbf{r}$ is the nondivergent symmetric part of the mean mass mixture velocity-gradient tensor.

For steady shear flow, the energy supplied to the grains by continuous shearing is balanced by the energy dissipation due to inelastic collisions, and Eq. (A9) reduces to the following form:

$$0=\sum_{m=l}^{d}\left\{\rho^ma_{\langle xy\rangle}^{\dagger m}+\sum_{p=l}^{d}(1+e_0)\rho^mn^p\sigma^3g_c^{mp}\left[\frac{\pi}{15}(a_{\langle xy\rangle}^{\dagger m}+a_{\langle xy\rangle}^{\dagger p})-\tfrac{2}{15}\sigma(\pi T)^{1/2}\dot\varepsilon(z)\right]\right\}\dot\varepsilon(z)+\sum_{m=l}^{d}\sum_{p=1}^{d}2\rho^m\sigma^2(1-e_0^2)g_c^{mp}n^pT(\pi T)^{1/2}. \tag{A14}$$

In the above equation, $\dot\varepsilon(z)$ is the local rate of shear.

Expressions for the pressure deviators $a_{\langle xy\rangle}^{\dagger l}$ and $a_{\langle xy\rangle}^{\dagger d}$ are given as follows:

$$\sum_{p=1}^{d}\sigma^2(1+e_0)g_c^{pn}n^p\rho^n(\pi T)^{1/2}\langle\{\tfrac{2}{3}+\tfrac{1}{5}[2+(1-e_0)]\}a_{\langle xy\rangle}^{\dagger n}+\{\tfrac{1}{5}[2+(1-e_0)]-\tfrac{2}{3}\}a_{\langle xy\rangle}^{\dagger p}\rangle=-\rho^nT\Bigg\langle1+\sum_{p=1}^{d}\pi\sigma^3(1+e_0)g_c^{np}n^p\times\{-\tfrac{1}{5}[1+(1-e_0)]+\tfrac{1}{3}\}\Bigg\rangle\dot\varepsilon(z),\quad n=l,d. \tag{A15}$$

Equation (A15) can be inserted into Eq. (A14) to obtain Eq. (15) for the mixture. It is worth mentioning that Eq. (A15) may be derived from the balance law for the deviant part of the mean of the second moment of velocity fluctuation, by assuming that the spatial gradients of the mean fields are small, and that the dimensionless quantities σ/L, $\sigma/t_0T_0^{1/2}$, $u^l/T_0^{1/2}$, $u^d/T_0^{1/2}$, $a^{\dagger l}/T_0$, $a^{\dagger d}/T_0$, $a^l/T_0^{1/2}$, and $a^d/T_0^{1/2}$ are all

of the same order of magnitude and small. Here, L, t_0, and T_0 are the characteristic length, time, and mixture granular temperature, respectively.

Assuming that $u_z^l \approx u_x^l \ll (u_x^l - u_x^d)$, and that $(u_x^l - u_x^d)T^{1/2}$ and $(a_x^l - a_x^d)T^{-1/2}$ are of the same order of magnitude, in the presence of nonuniform shear stress in the direction of shear gradient, namely, the z direction, the balances of momentum (A7) in the direction of the shear plane for particles of kind l, for which $n^l \gg n^d \approx n$, may be reduced to

$$\rho^l u_z^l = \frac{\partial}{\partial z}\left\{ \rho^l a_{\langle xz\rangle}^{\dagger l} + \sum_{p=l}^{d} (1+e_0)\rho^l n^p \sigma^3 g_c \left[\frac{\pi}{15}(a_{\langle xz\rangle}^{\dagger l} + a_{\langle xz\rangle}^{\dagger p}) - \tfrac{2}{15}\sigma (nT)^{1/2}\dot{\varepsilon}(z) \right] \right\}. \tag{A16}$$

Substituting for $a_{\langle xx\rangle}^{\dagger l}$ and $a_{\langle xx\rangle}^{\dagger d}$ from Eq. (A15), assuming that the parameter $T/\dot{\varepsilon}(z)^2$ does not change significantly in the direction of the shear gradient [62], gives a reduced form of this drift,

$$\rho^l u_z^l = -\left[\frac{\sigma T^{1/2}}{15\pi^{1/2}(3-e_0)\dot{\varepsilon}(z)^2} \right] \frac{\partial}{\partial z}(\rho^l U), \tag{A17}$$

where the term in the brackets, $B = \sigma T^{1/2}/15\pi^{1/2}(3-e_0)\dot{\varepsilon}(z)^2$, is the particle mobility and $U = \{2(1+e_0)g_c\Phi_s[18+3e_0(-2+\pi)-\pi]+5\pi\}\dot{\varepsilon}(z)^2$ is a potential field, which is a function of position. The term on the right side of Eq. (A17) represents the contribution of inhomogeneous shear to the drift as well as the extra diffusive flux arising from viscosity gradients.

[1] M. E. Cates, J. P. Wittmer, J.-P. Bouchaud, and P. Claudin, Phys. Rev. Lett. **81**, 1841 (1998).

[2] P. A. Thompson and G. S. Grest, Phys. Rev. Lett. **67**, 1751 (1991).

[3] C.-H. Liu, S. R. Nagel, D. A. Schecter, S. N. Coppersmith, S. Majumdar, O. Narayan, and T. A. Witten, Science **269**, 513 (1995).

[4] B. Miller, C. O'Hern, and R. P. Behringer, Phys. Rev. Lett. **77**, 3110 (1996).

[5] P. Pieranski, Am. J. Phys. **52**, 68 (1984); J. S. Olafsen and J. S. Urbach, Phys. Rev. Lett. **81**, 4369 (1998); G. Strassburger and I. Rehberg, Phys. Rev. E **62**, 2517 (2000).

[6] G. Ahmadi (private communication); more details including a geometrical description of the apparatus may be found in K. E. Elliott, G. Ahmadi, and W. Kvasnak, J. Non-Newtonian Fluid Mech. **74**, 89 (1998).

[7] H. M. Jaeger, S. R. Nagel, and R. P. Behringer, Phys. Today **49**(4), 32 (1996).

[8] N. Menon and D. J. Durian, Science **275**, 1920 (1997).

[9] P. A. Cundall and O. D. L. Strack, Geotechnique **29**, 47 (1979); K. Yamne, M. Nakagawa, S. A. Altobelli, T. Tanaka, and Y. Tsuji, Phys. Fluids **10**, 1419 (1998); C. M. Dury and G. H. Ristow, Europhys. Lett. **48**, 60 (1999).

[10] P. K. Haff, in *Granular Matter*, edited by Anita Mehta (Springer-Verlag, New York, 1994).

[11] B. J. Alder and T. Wainwright, J. Chem. Phys. **31**, 459 (1959).

[12] C. K. K. Lun and A. A. Bent, J. Fluid Mech. **258**, 335 (1994); C. S. Campbell, *ibid.* **348**, 85 (1997); P. Zamankhan, T. Tynjälä, W. Polashenski, Jr., P. Zamankhan, and P. Sarkomaa, Phys. Rev. E **60**, 7149 (1999).

[13] C. Bizon, M. D. Shattuck, J. B. Swift, W. D. McCormick, and H. L. Swinney, Phys. Rev. Lett. **80**, 57 (1998).

[14] M. D. Rintoul and S. Torquato, J. Chem. Phys. **105**, 9258 (1996); P. Zamankhan, H. Vahedi Tafreshi, W. Polashenski, Jr., P. Sarkomaa, and C. L. Hyndman, *ibid.* **109**, 4487 (1998).

[15] P. J. Steinhardt, D. R. Nelson, and M. Ronchetti, Phys. Rev. B **28**, 784 (1983).

[16] At short times, namely, before collisions occur, a particle diffuses as a free particle and $\langle \Delta \mathbf{r}^2(t)\rangle$ grows as t^2. At long times, after many collisions, $\langle \Delta \mathbf{r}^2(t)\rangle$ grows as t, where the Einstein relation, namely, $\langle \Delta \mathbf{r}^2\rangle = 6tD$, is obeyed. Here, D represents the coefficient of self-diffusion that characterizes, on average, the dissipation of spontaneous density fluctuations produced by local aggregation and redispersion of particles. The dynamics of density fluctuations may be monitored by calculating of the self-space-time correlation function $G_s(\mathbf{r},t)$, which involves features of the radial distribution function combined with features of time correlation functions.

[17] P. Zamankhan, W. Polashenski, Jr., H. Vahedi Tafreshi, A. Shakib Manesh, and P. Sarkomaa, Phys. Rev. E **58**, R5237 (1998).

[18] J. Bridgwater, in *Granular Matter* (Ref. [10]).

[19] A. Einstein, Ann. Phys. (Leipzig) **17**, 549 (1905).

[20] N. Menon (private communication).

[21] V. V. R. Natarajan, M. L. Hunt, and E. D. Taylor, J. Fluid Mech. **304**, 1 (1995).

[22] C. Denniston and H. Li, Phys. Rev. E **59**, 3289 (1999).

[23] S. B. Savage and R. Dai, Mech. Mater. **16**, 225 (1993).

[24] J.-P. Hansen and I. R. McDonald, *Theory of Simple Liquids* (Academic, New York, 1986).

[25] P. Zamankhan, Phys. Rev. E **52**, 4877 (1995).

[26] J. M. Kincaid, E. D. G. Cohen, and M. Lopez de Haro, J. Chem. Phys. **86**, 963 (1987); P. Zamankhan, Acta Mech. **123**, 235 (1997); B. O. Arnarson and J. T. Willits, Phys. Fluids **10**, 1324 (1998).

[27] P. C. Johnson and R. J. Jackson, J. Fluid Mech. **176**, 67 (1987).

[28] G. Boffetta, V. Carbone, P. Dgiuliani, P. Veltri, and A. Vulpiani, Phys. Rev. Lett. **83**, 4662 (1999).

[29] D. M. Hanes and D. L. Inman, J. Fluid Mech. **150**, 357 (1985).

[30] R. G. Horn and J. N. Israelachvili, J. Chem. Phys. **75**, 1400 (1981); D. Y. C. Chan and R. G. Horn, *ibid.* **83**, 5311 (1985); J. N. Israelachvili, P. M. McGuiggan, and A. M. Homola, Science **240**, 189 (1988); J. Van Alsten and S. Granick, Phys. Rev. Lett. **61**, 2570 (1988); R. G. Horn, S. J. Hirz, G. Hadziioannou, C. W. Frank, and J. M. Catala, J. Chem. Phys. **90**, 6767 (1989); M. L. Gee, P. M. McGuiggan, J. N. Israelachvili, and A. M. Nomola, *ibid.* **93**, 1895 (1990); P. A. Thompson and M. Robbins, Science **250**, 792 (1990).

[31] See EPAPS Document No. E-PLEEE8-66-084208 for the aforementioned appendix. This document may be retrieved via

the EPAPS homepage (http://www.aip.org/pubservs/epaps.html) or from ftp.aip.org in the directory lepapsl. See the EPAPS homepage for more information.
[32] W. A. M. Morgado and I. Oppenheim, Phys. Rev. E **55**, 1940 (1997).
[33] N. V. Brilliantov, F. Spahn, J. M. Hertzsch, and T. Pöschel, Phys. Rev. E **53**, 5382 (1996).
[34] W. Goldsmith, *Impact: The Theory and Physical Behaviour of Colliding Solids* (Arnold, London, 1960).
[35] T. Schwager and T. Pöschel, Phys. Rev. E **57**, 650 (1998).
[36] M. P. Allen and D. J. Tildesley, *Computer Simulation of Liquids* (Clarendon, Oxford, 1997).
[37] C. K. K. Lun and S. B. Savage, J. Appl. Mech. **54**, 47 (1987).
[38] C. A. Coulomb, Acad. R. Sci. Mem. Math. Phys. Par Divers Savants **7**, 343 (1773).
[39] J. T. Jenkins and M. W. Richman, Phys. Fluids **28**, 3485 (1985).
[40] D. Gugan, Am. J. Phys. **68**, 920 (2000).
[41] A. E. H. Love, *A Treatise on the Mathematical Theory of Elasticity* (Dover, New York, 1944).
[42] K. J. Johnson, *Contact Mechanics* (Cambridge University Press, Cambridge, 1987).
[43] A. W. Lees and S. F. Edwards, J. Phys. C **5**, 1921 (1972).
[44] W. Loose and G. Ciccotti, Phys. Rev. A **45**, 3859 (1992).
[45] A. Goldshtein, M. Shapiro, and C. J. Gutfinger, J. Fluid Mech. **316**, 29 (1996).
[46] C. K. K. Lun and S. B. Savage, Acta Mech. **63**, 15 (1986).
[47] T. G. Drake, J. Fluid Mech. **225**, 121 (1991).
[48] H. S. Carslaw and J. C. Jaeger, *Conduction of Heat in Solids* (Clarendon, Oxford, 1976).
[49] F. G. Bridges, A. Hatzes, and D. N. C. Lin, Nature (London) **309**, 333 (1984).
[50] J. R. Dormand and P. J. Prince, J. Comput. Appl. Math. **6**, 19 (1980).
[51] J. W. Dally and W. F. Riley, *Experimental Stress Analysis* (McGraw-Hill, Tokyo, 1978).
[52] J. O. Hirschfelder, C. F. Curtiss, and R. B. Bird, *Molecular Theory of Gases and Liquids* (Wiley, New York, 1954).
[53] A. Rahman, Phys. Rev. Lett. **32**, 52 (1974).
[54] B. Miller, Ph.D. thesis, Duke University, 1997, p. 54.
[55] P. A. Thompson and M. O. Robbins, Science **250**, 792 (1990).
[56] C. H. Liu, S. R. Nagel, D. A. Schecter, S. N. Coppersmith, S. Majumdar, O. Narayan, and T. A. Witten, Science **269**, 513 (1995).
[57] M. Farge, Annu. Rev. Fluid Mech. **24**, 395 (1992); I. Daubechies, *Ten Lectures on Wavelets* (SIAM, Montpelier, Vermont, 1992).
[58] R. Kronald-Martinet, J. Morelet, and A. Grossmann, Int. J. Pattern Recognit. Artif. Intell. **1**, 273 (1987).
[59] S. Chapman and T. G. Cowling, *The Mathematical Theory of Non-Uniform Gases* (Cambridge University Press, Cambridge, 1970).
[60] H. van Beijeren and M. H. Ernst, Physica (Amsterdam) **68**, 437 (1973).
[61] H. Grad, Commun. Pure Appl. Math. **2**, 331 (1949).
[62] S. S. Hsiau and M. L. Hunt, J. Fluid Mech. **251**, 299 (1993).